

# Quantum-Enhanced Neural Exchange-Correlation Functionals

Igor O. Sokolov,<sup>1,\*</sup> Gert-Jan Both,<sup>1</sup> Art D. Bochevarov,<sup>2</sup> Pavel A. Dub,<sup>3</sup> Daniel S. Levine,<sup>2</sup> Christopher T. Brown,<sup>4</sup> Shaheen Acheche,<sup>1</sup> Panagiotis Kl. Barkoutsos,<sup>1</sup> and Vincent E. Elfving<sup>1</sup>

<sup>1</sup>PASQAL, 2 av. Augustin Fresnel, Palaiseau 91120, France

<sup>2</sup>Schrödinger Inc., 1540 Broadway, 24th Floor, New York, NY 10036, United States

<sup>3</sup>Schrödinger Inc., 9868 Scranton Rd Suite 3200, San Diego, CA 92121, United States

<sup>4</sup>Schrödinger Inc., 1 Main St 11th Floor, Cambridge, MA 02142, United States

(Dated: April 23, 2024)

Kohn-Sham Density Functional Theory (KS-DFT) provides the exact ground state energy and electron density of a molecule, contingent on the as-yet-unknown universal exchange-correlation (XC) functional. Recent research has demonstrated that neural networks can efficiently learn to represent approximations to that functional, offering accurate generalizations to molecules not present during the training process. With the latest advancements in quantum-enhanced machine learning (ML), evidence is growing that Quantum Neural Network (QNN) models may offer advantages in ML applications. In this work, we explore the use of QNNs for representing XC functionals, enhancing and comparing them to classical ML techniques. We present QNNs based on differentiable quantum circuits (DQCs) as quantum (hybrid) models for XC in KS-DFT, implemented across various architectures. We assess their performance on 1D and 3D systems. To that end, we expand existing differentiable KS-DFT frameworks and propose strategies for efficient training of such functionals, highlighting the importance of fractional orbital occupation for accurate results. Our best QNN-based XC functional yields energy profiles of the H<sub>2</sub> and planar H<sub>4</sub> molecules that deviate by no more than 1 mHa from the reference DMRG and FCI/6-31G results, respectively. Moreover, they reach chemical precision on a system, H<sub>2</sub>H<sub>2</sub>, not present in the training dataset, using only a few variational parameters. This work lays the foundation for the integration of quantum models in KS-DFT, thereby opening new avenues for expressing XC functionals in a differentiable way and facilitating computations of various properties.

## I. INTRODUCTION

Density Functional Theory (DFT) has emerged as a major direction of research in modern quantum chemistry, enabling an efficient prediction of the electronic structure and properties of molecules and materials.<sup>1–3</sup> It has become the dominant method for solving the Schrödinger equation in physics-based atomistic simulations.<sup>4,5</sup> DFT's effectiveness largely stems from the ability to express the ground state density of interacting electrons via a system of non-interacting electrons, the so-called Kohn-Sham system. However, DFT can yield exact ground state energy and electron density only if the exact exchange-correlation (XC) functional is provided. Despite the widespread applicability of the technique, the development of accurate and versatile DFT XC functionals remains a challenge.<sup>6–8</sup> Consequently, DFT faces problems such as underestimation of reaction barriers, band gaps<sup>9</sup>, and poor handling of degenerate states potentially due to delocalization and static correlation errors.<sup>10,11</sup> The universal functional capable of solving the aforementioned problems and capturing the diverse electronic properties of molecules, solids and surfaces remains unknown. In its pursuit, hundreds of approximate XC functionals have been devised.<sup>12,13</sup> Many of these XC functionals are tailored to certain types of chemical systems and properties thereof, and often require prior knowledge of the targeted data to ensure the success of the method.<sup>14–16</sup> An additional challenge when constructing such functionals lies in achieving a good balance

between accuracy and computational efficiency.<sup>17,18</sup>

A number of recent studies<sup>19–27</sup> propose the use of compelling capabilities of machine learning (ML) techniques as a solution for the efficient design of XC functionals that can be used for generic DFT calculations. ML algorithms, ranging from deep neural networks to sophisticated regression models, have demonstrated their potential to unlock hidden patterns in vast datasets of chemical systems, allowing for the estimation of a universal XC functional. This combination of quantum chemistry and artificial intelligence heralds a promising era for XC functional design with many demonstrations for different systems<sup>28,29</sup> indicating the increase of the reach of the DFT methods. The majority of these ML-based techniques leverage differentiable programming as a widely used paradigm in deep learning (DL) that involves optimizing parameters with gradient-based methods.<sup>30</sup> In particular, existing chemistry codes are being refactored to incorporate automatic differentiation.<sup>31,32</sup> Training neural XC functionals within a differentiable DFT procedure was shown to provide superior generalization capabilities in 1D<sup>25,33</sup> compared to the previous approach.<sup>34</sup> Extensions to 3D with variation of model inputs (e.g., density with its gradients), locality<sup>28,32</sup> and novel genetic approaches<sup>35</sup> followed, to name just a few. Nevertheless, a universal neural XC functional has not been trained yet.<sup>30</sup> In an effort to meet this challenge, we propose a novel method for learning representations of XC functionals.

Recently, a novel DL framework within the broader

scope of quantum machine learning (QML) has been introduced.<sup>36</sup> This framework utilizes differentiable quantum circuits (DQCs), capitalizing on the unique methodologies inherent in quantum computation. This category of circuits facilitates the construction of quantum neural networks (QNNs), enabling efficient function representation<sup>37</sup> and derivative computation through analytic differentiation rules.<sup>38–40</sup> Various QNN models, which utilize different data encoding methods and distinct quantum circuit designs, have emerged.<sup>41</sup> A relevant quantum advantage in QML has been shown for situations where purely quantum data (quantum state) is used as the model input<sup>42</sup> and when the quantum model is learning from quantum experiments.<sup>43</sup> However, given the predominance of classical data in ML, the appeal of QNNs lies in their high effective dimension and rich expressivity,<sup>37</sup> which are determined by the unitary mappings of data to quantum states.<sup>44</sup> Despite sharing many issues with classical neural networks, such as problems with barren plateaus,<sup>45</sup> as well as unique issues such as the absence of efficient backpropagation,<sup>46</sup> advances have been made in addressing these through specific techniques<sup>47,48</sup> and efficient output extraction methods.<sup>49,50</sup> Recently, geometric DL has been extended to QML, introducing graph-based<sup>51–57</sup> and equivariant QNNs.<sup>58–62</sup> These adaptations come with theoretical assurances against barren plateaus<sup>63</sup> and constraints on overparametrization, contingent upon adherence to fixed symmetries.<sup>59</sup> Yet, overly symmetrical quantum models risk becoming efficiently simulatable by classical methods.<sup>64</sup> Hence, only intelligently-designed QNNs can surmount previously mentioned challenges and capitalize on their enhanced expressivity.

Many studies have explored the combination of DFT with variational quantum algorithms through auxiliary Hamiltonians,<sup>65</sup> embedding schemes,<sup>66</sup> or reduced density matrix methods,<sup>67</sup> among others. However, to the best of our knowledge, the direct application of QML for the functional representation of XC has not been explored. Therefore, in this work, we investigate the synergy between QML and DFT for designing XC functionals.<sup>68</sup> The goal is to use techniques arising from the QML domain to process empirical data from DFT (or general quantum chemistry) calculations within the supervised ML approach to create more robust and versatile XC functionals that can be applied to a wider range of problems in the quantum chemistry domain. Our main contributions are:

- (i) the expansion of KS-DFT frameworks for quantum XC functional training,
- (ii) a demonstration of fractional occupation's importance in 3D KS-DFT for accuracy,
- (iii) the introduction of QNNs models for XC representation, showcasing efficiency in 1D and 3D, and
- (iv) a demonstration that quantum models can potentially be more parameter-efficient than classical

ones.

This work is structured as follows: In Sec. II, we give the theoretical background of QML for KS-DFT and define our models for XC functionals. In Sec. III, we provide details of our framework implementation. In Sec. IV, we present our empirical study of the proposed architectures and discuss the required quantum resources. Finally, in Sec. V, we discuss our conclusions and give an outlook on the development of useful quantum-enhanced XC functionals.

## II. THEORY

In this section, we introduce the KS-DFT approach, which serves as the foundation for training and evaluating our (quantum) machine-learned XC functionals. Subsequently, we delve into the utilization of (quantum) ML for training XC functionals. We discuss how neural XC functionals are embedded in KS-DFT and their architectural details.

### A. Kohn-Sham Density Functional Theory

Contemporary KS-DFT implementations<sup>2</sup> achieve the electronic ground state through a solution of the KS equations

$$\hat{H}[n](\mathbf{r})\phi_i(\mathbf{r}) = \epsilon_i\phi_i(\mathbf{r}), \quad (1)$$

to self-consistency with respect to the electronic density  $n(\mathbf{r})$ . The Hamiltonian operator is given by  $\hat{H}[n](\mathbf{r}) = -\nabla^2/2 + v_{\text{KS}}[n](\mathbf{r})$  as a function of the electron density  $n(\mathbf{r})$ . The latter is defined as the sum of probability densities over all  $N_{\text{occ}}$  occupied orbitals,  $n(\mathbf{r}) = \sum_{i=1}^{N_{\text{occ}}} |\phi_i(\mathbf{r})|^2$ , where  $\phi_i$  is a one-electron KS orbital with corresponding energy  $\epsilon_i$ . The KS potential is given by  $v_{\text{KS}}[n](\mathbf{r}) = v(\mathbf{r}) + v_{\text{H}}[n](\mathbf{r}) + v_{\text{XC}}[n](\mathbf{r})$ , which contains the external ionic Coulomb potentials  $v(\mathbf{r})$ , the Hartree potential  $v_{\text{H}}[n](\mathbf{r})$ , and the XC potential  $v_{\text{XC}}[n](\mathbf{r})$ . The XC potential is the functional derivative of the XC energy,  $E_{\text{XC}}$ , with respect to the electron density, i.e.  $v_{\text{XC}}[n](\mathbf{r}) = \delta E_{\text{XC}}[n]/\delta n(\mathbf{r})$ . The XC energy  $E_{\text{XC}}$  is defined as

$$E_{\text{XC}}[n] = \int d\mathbf{r} \epsilon_{\text{XC}}[n](\mathbf{r})n(\mathbf{r}), \quad (2)$$

where  $\epsilon_{\text{XC}}[n](\mathbf{r})$  is the XC energy per electron. Finally, the total energy is obtained as the sum,  $E[n] = T_S[n] + V[n] + E_{\text{H}}[n] + E_{\text{XC}}[n]$ , of the kinetic energy  $T_S[n]$ , the external potential energy  $V[n]$ , the Hartree energy  $E_{\text{H}}[n]$  and the XC energy  $E_{\text{XC}}[n]$ .

In practice, given a finite basis set  $\{\xi_i\}_{i=1}^{N_b}$ , a linear combination of  $N_b$  basis functions,  $\phi_i(\mathbf{r}) = \sum_{j=1}^{N_b} p_j^i \xi_j(\mathbf{r})$ , is optimized to produce suitable orbitals  $\phi$ . This involves the solution of Roothan's equation defined as

$$\mathcal{F}[n]\mathbf{p}_i = \epsilon_i S \mathbf{p}_i, \quad (3)$$

where  $\mathbf{p}_i = (p_i^1, \dots, p_i^{N_b})^T$ ,  $S_{ij} = \int d\mathbf{r} \xi_i(\mathbf{r}) \xi_j^*(\mathbf{r})$  is the overlap matrix and  $\mathcal{F}[n]$  is the Fock matrix as a functional of the electron density profile  $n$ , with elements  $\mathcal{F}_{ij} = \int d\mathbf{r} \xi_i(\mathbf{r}) H[n](\mathbf{r}) \xi_j^*(\mathbf{r})$ . Eq. (3) is then solved, e.g., numerically by an eigendecomposition of the Fock matrix to obtain the orbital coefficients  $\{\mathbf{p}_i\}$  that correspond to some density profile  $n$ . Self-consistency is achieved when the electron density no longer changes within a specified tolerance within fixed  $N_{KS}$  KS iterations (solutions of Eq.(3)). The resulting energy  $E$  can then be compared to validated experimental data, with the quality of the result dependent on the choice of the (neural) functional used to represent  $E_{XC}[n]$ . If the exact XC functional was known, Hohenberg-Kohn theorems<sup>69</sup> guarantee that the self-consistent solution yields the exact ground-state energy and density.

## B. Embedding of neural XC functionals within KS-DFT

Within the established Kohn-Sham framework, neural XC models are integrated using Eq. (2). They are represented by differentiable functions  $f_\theta : (n, \mathbf{r}) \rightarrow \epsilon_{XC}(\mathbf{r})$  with parameters denoted by  $\theta$ . Consequently, the machine-learned XC energy can be expressed in general as  $E_{XC}[n] \approx E_{XC}^\theta[n] = \int d\mathbf{r} f_\theta(n, \mathbf{r}) n(\mathbf{r})$ , where  $E_{XC}^\theta[n]$  approximates the exact  $E_{XC}[n]$ . In practice, an integration grid is used to compute the integral on a finite educated choice of  $N_{grid}$  grid points. In general, the XC energy is integrated as

$$E_{XC}[n] \approx E_{XC}^{\theta,1}[n] = \sum_{i=1}^{N_{grid}} w_i f_\theta(n, \mathbf{r}_i) n(\mathbf{r}_i), \quad (4)$$

where the grid weights  $\{w_i\}_{i=1}^{N_{grid}}$  are computed for each grid type and chemical system. The values  $\{\mathbf{r}_i\}_{i=1}^{N_{grid}}$  denote the Cartesian coordinates associated with grid points. We call this scheme the *local energy embedding* since local XC energy density  $\epsilon_{XC}(\mathbf{r})$  is required (see Fig. 2(a)). Another approach is to represent the total XC directly with a neural functional  $F_\theta[n]$ , bypassing the integration as

$$E_{XC}[n] \approx E_{XC}^{\theta,2}[n] = F_\theta[n], \quad (5)$$

where  $F_\theta[n]$  learns implicitly the relation between the XC energy and the grid during training through  $\{n_i\}_{i=1}^{N_{grid}}$  input density values. Both equations, Eqs. (4) and (5), provide distinct ways of embedding neural networks as XC functionals in KS-DFT frameworks. We call this approach the *global energy embedding* since the model requires the whole density profile to infer the total XC energy (see Fig. 2(a)). Note that despite avoiding grid integration in the global energy embedding, both techniques require the computation of the local XC potential  $v_{XC}[n](\mathbf{r})$  at every grid point.

## C. Architectures of neural XC functionals

In this section, we propose a blueprint of basic model architectures that can couple classical and quantum layers. In general, neural XC functionals are represented by layers of (Q)NNs that are compositions of differentiable functions,

$$f_\theta(n, \mathbf{r}) = (f_{\theta_{N_l}}^{N_l} \circ f_{\theta_{N_{l-1}}}^{N_{l-1}} \circ \dots \circ f_{\theta_1}^1)(n, \mathbf{r}), \quad (6)$$

with parameters  $\theta = (\theta_{N_l}, \dots, \theta_1)$  and  $N_l$  layers.

In Sec. II B, it was shown that both *local* and *global* energy embeddings can be used to integrate such models in KS-DFT. Neural XC functionals are also characterized by various degrees of *locality* that represents the number of density points provided as inputs.<sup>70</sup> Locality was shown to greatly impact the ability to learn accurate XC functionals.<sup>25</sup> In particular, *1-local* models are represented by the functions  $f_\theta^{\text{local}} : n_i \rightarrow \epsilon_{XC,i}^\theta$ , where the model function has access only to a single local density information and is applied in succession on  $N_{grid}$  points. This function is embedded in DFT via Eq. (4). *L-local* models are represented by the functions

$$f_\theta^{\text{local}} : \{n\}^L \rightarrow \epsilon_{XC,i}^\theta, \quad (7)$$

where the model function has access only to some  $L$  neighboring density points (kernel size) at a time and is applied in succession on, e.g.,  $\lceil N_{grid}/L \rceil$  points.<sup>70</sup> Similarly to local models, this type of function is embedded in DFT via Eq. (4). *Global* models are defined as a functional of the whole density,

$$F_\theta^{\text{global}} : \{n\}_{i=1}^{N_{grid}} \rightarrow E_{XC}^\theta, \quad (8)$$

where the NN represents the whole integrated XC energy and is embedded in DFT via Eq. (5). Alternatively, global models can also be embedded in DFT via Eq. (4) as

$$f_\theta^{\text{global}} : \{n\}_{i=1}^{N_{grid}} \rightarrow \{\epsilon_{XC,i}^\theta\}_{i=1}^{N_{grid}}, \quad (9)$$

where local XC energy density depends on the whole electron density. Next, we present the concrete realisation of our XC models in classical and quantum settings.

### 1. Classical architectures

The most general NN is a Multilayer Perceptron (MLP) model, where the layers are given by  $f_{\theta_k}^k(\mathbf{n}, \mathbf{r}) = \alpha(A\mathbf{n} + \mathbf{b})$  with an activation function  $\alpha$  and trainable matrix  $A$  and vector  $\mathbf{b}$ . Theoretically, given enough layers, MLPs can represent any function, as per the universal approximation theorem<sup>71</sup>. The practical use of MLPs as effective ML models is hindered by the large number of parameters and the lack of inductive biases. This can lead to overfitting to the training data and poor generalization to data outside the training set. Since we are

exploring the most general quantum models, MLPs are suitable candidates for comparative studies. To achieve this goal, we implement MLP models that have  $N_i$  inputs and  $N_l$  layers consisting of  $N_n$  neurons. We introduce the local and global versions of the MLP model. Local MLP (LMLP) is defined as

$$f_\theta^{\text{LMLP}} : n_i \rightarrow \epsilon_{\text{XC},i}^\theta, \quad (10)$$

using Eq. (7), where the model function has access only to the local density information and is applied on  $N_{\text{grid}}$  points. This function is embedded in DFT via Eq. (4). Note that  $L$ -local MLPs, where not a single density value  $n_i$  but a collection of  $L$  neighboring densities  $\{n_i\}^L$  are taken as input, were already investigated in ref.<sup>70</sup>. The global version of the MLP, Global MLP (GMLP), is defined as a functional of the whole density,

$$F_\theta^{\text{GMLP}} : \{n\}_{i=1}^{N_{\text{grid}}} \rightarrow E_{\text{XC}}^\theta, \quad (11)$$

using Eq. (8), and is embedded in the DFT theory using Eq. (5). Amongst more elaborate NNs, the Global Kohn-Sham Regularizer (GKSR) model<sup>25</sup> is one of the best models for the XC energy.<sup>25,30</sup> Combining local and global convolutional layers, GKSR incorporates inductive biases such as a self-interaction gate and a negativity transform, addressing common issues like self-interaction errors and imposing the negativity condition on the XC energy.<sup>25</sup> In our implementation, the GKSR model is represented by the function:

$$f_\theta^{\text{GKSR}} : \{n\}_{i=1}^{N_{\text{grids}}} \rightarrow \{\epsilon_{\text{XC},i}^\theta\}_{i=1}^{N_{\text{grids}}} \quad (12)$$

using Eq. (9). Note that despite representing a global functional, it is embedded in DFT via Eq. (4), unlike GMLP. This allows us to showcase the results of embedding these XC models in DFT using both Eq.(4) (local/global) and Eq.(5) (global). In the following section, we discuss how XC functionals can be represented as quantum circuits.

## 2. Quantum architectures

A widely adopted strategy for QML models involves the utilization of a QNN, typically constructed using differentiable quantum circuits.<sup>36</sup> In this work, our quantum XC functionals are based on such QNNs, which consist of three blocks: a feature map  $U_f$ , an ansatz  $U_a$  and a measurement of an operator  $\hat{O}$ . Typically, a  $N_q$ -qubit quantum computer is initialized at some initial state  $|0\rangle$ . Here we consider the zero computational basis state on all qubits. A feature map is used to embed the data (e.g., electron density  $n$ ) in the Hilbert space,  $U_f(n)|0\rangle$  in a differentiable manner for the computation of XC potential  $v_{\text{XC}}$ . The discretized density  $\{n\}_{i=1}^{N_{\text{grids}}}$  values are embedded in the feature map as gate parameters. Then, an ansatz circuit  $U_a(\theta_a)$  is used to act on the embedded data with local qubit operations and entangling gates

that mediate interactions to represent the most general action on the data. Finally, the output of the model is extracted via projective measurements (shots) of an arbitrary cost operator  $\hat{C} = \sum_{i=1}^{N_o} \theta_c^i \hat{O}_i$ , where  $\theta_c$  are fixed or trainable parameters associated with Pauli operators  $\hat{O} \in \{I, \hat{X}, \hat{Y}, \hat{Z}\}^{\otimes N_q}$ . We assume the parameters  $\theta_c$  are non-trainable, unless specified otherwise. The cost operator is chosen to be total magnetization,  $\hat{C} = \sum_{i=1}^{N_q} \hat{Z}_i$ , which was shown to avoid cost-function-induced barren plateaus<sup>72</sup>. The representation of such model is given by a function

$$f_\theta^q(n) = \langle 0 | U^\dagger(n, \theta) \hat{C} U(n, \theta) | 0 \rangle, \quad (13)$$

where  $U(n, \theta) = \prod_{l=1}^{N_l} \left( \prod_{d=1}^{N_d} U_a^{l,d}(\theta_a^{l,d}) U_f^l(n) \right)$  is the general representation of the model with  $N_d$  ansatz layers and  $N_l$  total repetition of ansatz and feature map, which implements the data re-uploading strategy.<sup>73</sup> The repetitions of layers are akin to the number of layers of classical NNs and augment the expressivity of the model. Given enough layers, classical and quantum models can, in principle, approximate a given function.<sup>71,73,74</sup> In Appendix C, we give details of typical building blocks of QNNs.

To parallel the local MLP, we formulate a fully Local QNN (LQNN) designed to take a single density point  $n_i$  as input and yield the expectation of an observable:

$$f_\theta^{\text{LQNN}} : n_i \rightarrow \epsilon_{\text{XC},i}^\theta = \langle 0 | U^\dagger(n_i, \theta) \hat{C} U(n_i, \theta) | 0 \rangle, \quad (14)$$

defined through Eq. (7) and integrated into DFT via Eq. (4). We explore local QNNs with both product (Eq. (C5)) and Chebyshev (Eq. (C6)) feature maps, named Local PrQNN and Local ChQNN, respectively. The ansatz adheres exactly to the structure specified in Eq. (C3). Note that for this model it is possible to consider  $L$ -local case,  $f_\theta^{\text{LQNN}} : \{n_i\}^L \rightarrow \epsilon_{\text{XC},i}^\theta = \langle 0 | U^\dagger(n, \theta) \hat{C} U(n, \theta) | 0 \rangle$ , where a collection of  $L$  neighboring densities is embedded in a single feature map. However, as shown in ref. 25, only global functional (e.g.,  $L = N_{\text{grid}}$ ) is capable of best approximating exact XC functionals. Hence, in the next section, we develop model architectures that embed the whole density.

## 3. Quantum-classical hybrid architectures

We propose to leverage advantages of classical NNs and combine them with quantum models. Notably, the number of elements  $N_{\text{grid}}$  in the electron density  $\mathbf{n}$  scales linearly with the number of atoms.<sup>75</sup> Even for small diatomic molecules, there are hundreds of grid points for the smallest grid density available with the best integration grids<sup>75</sup>. This poses an issue with the feature maps based on angle encoding since the number of qubits  $N_q$  required to embed the entire density  $\mathbf{n}$  equals its size  $N_{\text{grid}}$ , posing severe requirements for potential implementation on near-term quantum computers. Hence, we devise a model, Global QNN (GQNN), that is composed of

two layers:

$$f_{\theta}^{\text{GQNN}}(n) = (f_{\theta_c}^c \circ f_{\theta_q}^q)(n), \quad (15)$$

where  $f^c$  and  $f^q$  represent the classical and quantum layers with associated parameters  $\theta_c$  and  $\theta_q$ , respectively. In principle, any differentiable classical layer can be used to map the outputs of  $f_{\theta_q}^q$  to XC energy. Here, the quantum layer consists of  $L$ -local QNNs defined as

$$f_{\theta}^q : \{n_i\}^L \rightarrow \epsilon_{\text{XC},i} = \langle 0 | U^\dagger(n, \theta) \hat{C} U(n, \theta) | 0 \rangle, \quad (16)$$

with a product feature map and an alternate ladder ansatz. We first partition the input  $\mathbf{n}$  in  $N_b = \lceil N_{\text{grid}} / L \rceil$  batches and then apply  $f_{\theta}^q$  to each batch. This results in  $N_b$  outputs that become the inputs of a classical function  $f_c$  defined as

$$f_{\theta_c}^c : \{\epsilon_{\text{XC},i}\}_{i=1}^{N_b} \rightarrow E_{\text{XC}}^{\theta}, \quad (17)$$

where, for simplicity, the classical layer is the standard MLP with  $N_b$  input neurons and one output neuron (potentially with additional MLP layers). In general, any classical model architecture can be used to represent the classical layer.

#### 4. Quantum-inspired architectures

Another possibility for designing XC functionals is to use simulated quantum models as quantum-inspired (Qi) solution. We introduce the Global QiNN, which incorporates density through amplitude embedding (Eq. (C4)) and utilizes the standard ansatz outlined in earlier sections. It is represented by the function

$$F_{\theta}^{\text{QiNN}} : (\{n\}_{i=1}^{N_{\text{grid}}}) \rightarrow E_{\text{XC}}^{\theta}, \quad (18)$$

where amplitude embedding feature map is used.

Finally, we propose Global Quantum-inspired Convolutional NN (GQiCNN) architecture that implements the composition of quantum layers with angle embedding as

$$f_{\theta}^{\text{GQiCNN}}(n) = (f_{\theta_c}^c \circ f_{\theta_{N_l}}^{q,N_l} \circ \dots \circ f_{\theta_{q,1}}^{q,1})(n), \quad (19)$$

where the product feature map (Eq. (C5)) is throughout all the layers. We do not employ Chebyshev embedding (Eq. (C6)) due to detrimental normalization of the data required, which suppresses the information about the number of electrons in our architectures. Similarly to the hybrid architecture (GQNN), we consider quantum layers that consist of  $L$ -local QNNs, defined in Eq. (16), with a product feature map and alternate ladder ansatz defined in Appendix C. The input is partitioned in  $\mathbf{n}$  in  $N_b = \lceil N_{\text{grid}} / L \rceil$  batches and then  $f_{\theta}^q$  is applied to each batch. This is repeated  $N_l$  times until the output is a single scalar, which represents  $E_{\text{XC}}$ . If not (i.e., odd number of inputs), the output of quantum layers is combined with an MLP as in Eq. (17) to output  $E_{\text{XC}}$ .

#### D. Reason for exploring quantum-enhanced models

What factors would encourage the adoption of quantum models? To answer this question, we can view quantum models as Fourier series. We examine feature maps like  $U_f(\mathbf{n}) = \bigotimes_{k=1}^{N_{\text{grid}}} e^{-i\varphi(n_k)\hat{G}_k}$ , covering all feature maps utilized in this study except for the amplitude encoding. For such feature maps, according to Schuld *et al.*<sup>44</sup>, Eq. (13) admits a Fourier series representation of the form:

$$f_{\theta}(\mathbf{n}) = \sum_{\mathbf{k}} \sum_{\mathbf{j}} c_{\mathbf{k},\mathbf{j}}(\theta_a, \hat{C}) e^{i\varphi(\mathbf{n}) \cdot \omega_{\mathbf{k},\mathbf{j}}}, \quad (20)$$

where  $\mathbf{i}, \mathbf{j} \in [2^{N_q}]^{N_{\text{grid}}}$  denote multi-indices,  $\omega_{\mathbf{k},\mathbf{j}} = \lambda_{\mathbf{k}} - \lambda_{\mathbf{j}}$  are Fourier frequencies,  $c_{\mathbf{j},\mathbf{k}}$  are Fourier coefficients and  $\varphi$  represents the element-wise  $\varphi$  acting on each element of the density  $\mathbf{n}$ . Schuld *et al.*<sup>44</sup> showed for the case  $\varphi(\mathbf{n}) = \mathbf{n}$  that the amplitudes  $c_{\mathbf{k},\mathbf{j}}$  only depend on the structure of the ansatz  $U_a$  and the cost operator  $\hat{C}$ . The frequencies  $\omega$  are determined by the eigenvalues  $\lambda$  of the generators in the feature map, where  $\hat{G}_k = \text{diag}(\lambda_1^{(k)}, \dots, \lambda_{2^{N_q}}^{(k)})$  are assumed to be diagonal, without loss of generality. The eigenvalues are combined in a vector as  $\lambda_{\mathbf{j}} = (\lambda_{j_1}^{(1)}, \dots, \lambda_{j_{N_{\text{grid}}}}^{(N_{\text{grid}})})$ . Detailed derivations can be found in Appendix of ref. 44. The important finding is that there are potentially  $2^{N_q}$  distinct modes composing the function  $f_{\theta}$ , which only depend on the choice of the feature map unitary  $U_f$ . In addition, despite attempts to classically approximate QNNs, which represent some function  $f_{\theta}$ , there is no reliable method for large  $N_q$  so far.<sup>76</sup> Hence, there is a potential quantum advantage in the ability to represent XC functionals (expressivity) by using an exponential number of Fourier modes given only  $N_q$  qubits on a quantum computer.

### III. METHODS

In this section, we discuss the implementation of our approach in differentiable chemistry frameworks and strategies for efficient training of neural XC functionals.

#### A. Implementation within differentiable chemistry frameworks

To evaluate the capabilities of quantum computers for machine learning XC functionals, we based our implementation on two differentiable frameworks.

Li *et al.* proposed an important method to facilitate the generalization of neural XC functionals: using the KS iterative procedure as a regularizer.<sup>25</sup> The novel idea is to compute the energy loss at every KS iteration and the electron density loss at the last KS iteration, and then to differentiate through  $N_{\text{KS}}$  iterations (solutions of Eq. (1)) which would enable the model to converge

faster to the reference, i.e., in fewer KS iterations, while regularizing its parameters. To allow this feature, a fully differentiable chemistry code in 1D in JAX<sup>77</sup> was developed<sup>25</sup> with the aim of demonstrating the regularization capacity of the framework.<sup>25</sup> Since it reduces the number of dimensions (to 1D) and hence simplifies the problem, this is an ideal setup for investigation of the capacity of QNN-based models to represent XC functionals. We adopt this exact framework with minimal changes to hyperparameters for all our preliminary results in 1D (i.e., only linear molecules).

However, realistic chemistry simulations require a full 3D treatment of molecular systems. To address this demand, Kasim *et al.* proposed a 3D differentiable chemistry framework implemented entirely in PyTorch<sup>78</sup>, which enabled accurate training of functionals for various diatomic systems.<sup>28</sup> However, both specialised frameworks of Li *et al.* and Kasim *et al.* are not used by computational chemists on a regular basis. Therefore, in this work, one of our goals is to contribute to an existing effort that focuses on making a popular chemistry framework, PySCF<sup>79</sup>, differentiable. This differentiable framework is known as PySCF with Automatic Differentiation (PySCFAD)<sup>31</sup>. It is similar to Li's 1D framework, as it is also based on JAX, but offers the capability for an accurate treatment of chemical systems in 3D, making it suitable for a wide range of chemical simulations. Working within the scope of the PySCFAD framework, we replaced the calls to the standard XC functionals in differentiable SCF calculations used in KS-DFT (see Sec. II) by (quantum) NNs. This entails that we introduce necessary modifications to the already well-tested KS-DFT implementation.

To facilitate the training of neural XC functionals within KS-DFT in 3D, the spin components of the electron density can be constrained to be equal, i.e.,  $n_{\uparrow}(\mathbf{r}) = n_{\downarrow}(\mathbf{r})$  and  $n(\mathbf{r}) = n_{\uparrow}(\mathbf{r}) + n_{\downarrow}(\mathbf{r})$ , which defines the so-called spin-restricted case of KS-DFT (RKS-DFT). Extending to the unrestricted case (UKS-DFT), which allows the treatment of open-shell systems, means transitioning from  $n(\mathbf{r})$  to  $(n_{\uparrow}(\mathbf{r}), n_{\downarrow}(\mathbf{r}))$  with corresponding potentials  $v_{XC,\sigma}[n_{\uparrow}, n_{\downarrow}](\mathbf{r}) = \delta E_{XC}[n]/\delta n_{\sigma}(\mathbf{r})$ , where spin states are denoted by  $\sigma = \{\uparrow, \downarrow\}$ . This modification doubles the number of inputs for the neural XC model,<sup>33</sup> adding complexity to its training. Hence, we focus on RKS-DFT.

In addition, standard RKS-DFT implementations fail to consistently represent the ground state density, preventing the training of accurate XC models. They assume that the ground state density  $n(\mathbf{r})$  can be accurately represented by a single determinant wave function of a non-interacting KS system with binary orbital occupation (0 or 1). However, the exact density of an interacting system, achievable theoretically via Full Configuration Interaction (FCI), allows for fractional occupation numbers.<sup>80</sup> To address this limitation, especially evident in the challenging strongly-correlated regime, we adopt the algorithm of Chai.<sup>81</sup> Other approaches can be employed with an increased computational cost.<sup>82</sup> Our

choice was dictated by the simplicity of its integration in existing codes, with detailed proofs given in ref. 81 and our implementation in Appendix A. See Figs. 1 and 2(a) for an overview of the complete method.

### Differentiable quantum-enhanced DFT framework

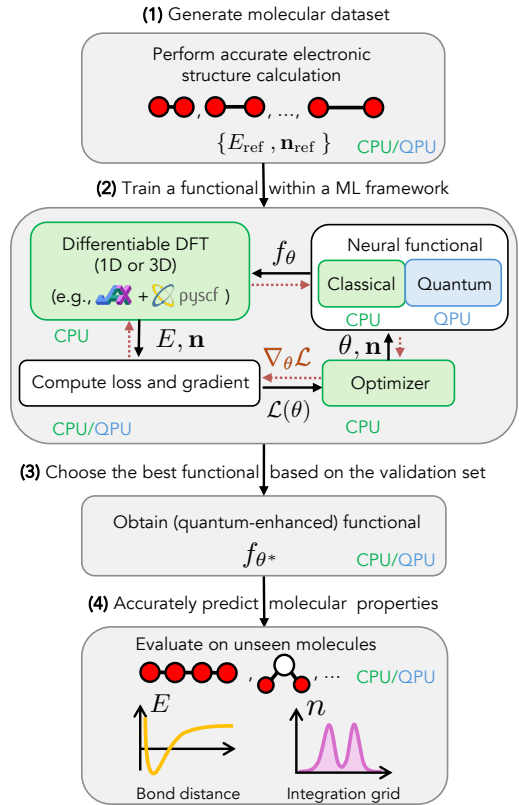


FIG. 1. Differentiable chemistry framework for training quantum-enhanced XC functionals. (1) The molecular dataset consists of reference energies  $E_{\text{ref}}$  and densities  $\mathbf{n}_{\text{ref}}$  generated by an accurate *ab initio* method. (2) A differentiable (Q)NN  $f_{\theta}$  outputs the XC energy. The corresponding potential is obtained via (automatic) differentiation. The Fock equations in KS-DFT are iteratively solved to obtain new orbitals until self-consistency. Each KS iteration contributes to the loss  $\mathcal{L}$ , resulting in regularization.<sup>25</sup> Trainable parameters  $\theta$  are updated by a classical optimizer. (3) The converged parameters  $\theta^*$  define the trained functional  $f_{\theta^*}$ , which is subsequently used to evaluate the properties of any molecule in stage (4). Brown arrows in (2) indicate the gradient flow through the procedure. CPU and QPU denote classical (i.e., central and graphical) and quantum processing units.

### B. Training neural XC functionals

In this work, we adopt the standard supervised ML approach. We generate the training (reference) dataset  $D = \{(E_{\text{ref}}^i, n_{\text{ref}}^i)\}_{i=1}^{N_{\text{mol}}}$  using an accurate *ab initio* method for  $N_{\text{mol}}$  different molecules (also including different geom-

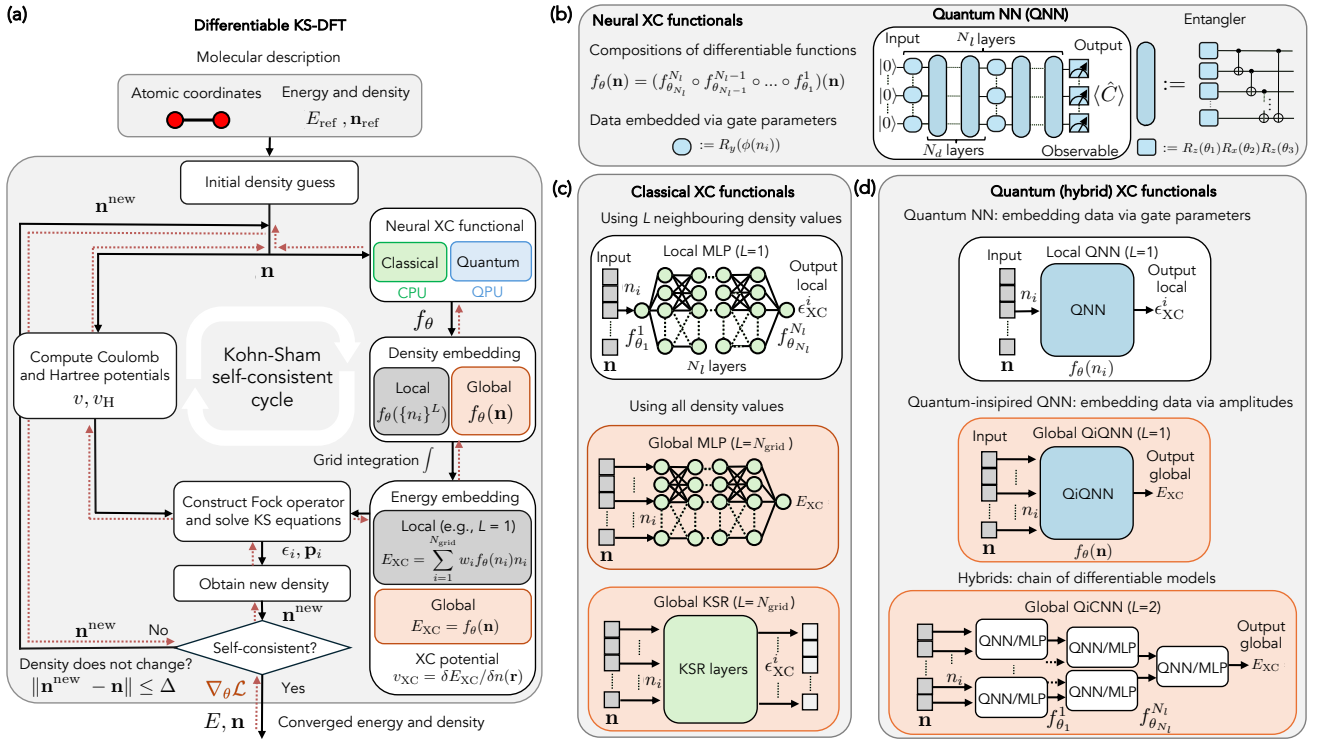


FIG. 2. (a) Method for training quantum-enhanced neural XC functionals within KS-DFT. Data describing a single molecule is passed to KS-DFT. An initial electron density  $\mathbf{n}$  estimate is made and potentials  $v, v_H$  and  $v_{XC}$  are computed to construct the Fock operator. Neural XC functional  $f_\theta$  is represented by a quantum and/or classical model, which takes  $L$  density values as inputs (i.e.,  $L = 1$  fully local and  $L = N_{\text{grid}}$  global). The XC functional can be embedded in DFT locally (outputs the values on every grid point) or globally (outputs the total XC energy). Then, the KS equation and the orbital coefficients  $\mathbf{p}$  are updated. The new density is computed and if the change is small enough, the procedure is stopped (self-consistency) and the trained XC functional is obtained. Otherwise, the new orbitals are kept for the next iteration. The loss function is computed and differentiated with respect to the model parameters. The red dashed arrows show the gradient flow. (b) Building blocks of neural XC functionals are defined as compositions of differentiable functions, which can be represented by QNNs. (c) Architectures of classical and (d) quantum (hybrid) XC functionals. Models differ by how many inputs can be taken at a time. The QiCNN architecture allows one to chain classical and quantum models. The orange color indicates that the global energy embedding (see (a)) is used, and the blue color indicates quantum operations. Note that MLPs can be replaced by any classical architecture.

tries of the same molecules). For the 1D implementation, we use the original training and test datasets by Li *et al.*<sup>25</sup> composed of hydrogen atom-based systems, e.g., H<sub>2</sub>, H<sub>2</sub>H<sub>2</sub> and H<sub>4</sub>. The data is obtained with DMRG simulations, where  $N_{\text{grid}} = 513$  is fixed for all the systems. For the 3D implementation, we use the PySCF software package and the coupled cluster singles and doubles (CCSD)<sup>83</sup> method to generate our data for H<sub>2</sub>, which is equivalent to FCI (an exact solution within a basis set) in this case. When more than two electrons are present, we suggest using the singles and doubles coupled cluster method with perturbative triples (CCSD[T]), which is viewed as the “gold standard” in computational chemistry.<sup>83</sup> A Gaussian-type orbital basis set, 6-31G, is used in all calculations. For an integration grid, we use SG-3 with a Becke scheme to combine multi-atomic grids, such that for a given molecule at all geometries we obtain the same number of grid points.<sup>75</sup> The grid density is set to minimum to reduce the number of neural XC functional

inputs, which simplifies the complexity of the problem. This entails  $N_{\text{grid}} = 1192$  for H<sub>2</sub> and  $N_{\text{grid}} = 2384$  for planar H<sub>4</sub> in the 3D setting. Given that we train models that allow only for a fixed number of inputs ( $N_{\text{grid}}$ ), grids have to be adapted (e.g., by pruning) to have the same number of grid points for all molecules in the dataset.<sup>75</sup> However, this is only a limitation imposed by simple prototypical (quantum) models that are investigated in this work. See Appendix B for additional clarifications about integration grids.

To train our models, we use the loss function given by

$$\begin{aligned} \mathcal{L}(\theta) = & \underbrace{\frac{1}{N_{\text{mol}}} \sum_{i=1}^{N_{\text{mol}}} \left[ \sum_{j=1}^{N_{\text{grid}}} w_j (n_{\text{KS},j}^i(\theta) - n_{\text{ref},j}^i)^2 / N_e^i \right]}_{\text{density loss } \mathcal{L}_n} \\ & + \underbrace{\frac{1}{N_{\text{mol}}} \sum_{i=1}^{N_{\text{mol}}} \left[ \sum_{k=1}^{N_{\text{KS}}} \eta_k (E_k^i(\theta) - E_{\text{ref}}^i)^2 / N_e^i \right]}_{\text{energy loss } \mathcal{L}_E}, \end{aligned} \quad (21)$$

where the expectation is taken on  $N_{\text{mol}}$  molecules of the training set,  $\eta_k$  weights the contribution of every energy at each KS iteration and  $w_j$  represents the integration grid weight. We use the weighting scheme introduced by Li *et al.*<sup>25</sup>:  $\eta_k = 0.9^{N_{\text{KS}}-k} H(k-10)$ , where  $H$  is the Heaviside function to tune the contribution of every loss term. All derivatives of the loss function are computed via JAX automatic differentiation in this work. On quantum hardware, exact differentiation schemes such as parameter-shift rule<sup>39</sup> or its generalized version<sup>40</sup> can be used (see Appendix D). The loss function is then minimized to obtain the optimal model parameters

$$\theta_{\text{opt}} = \text{argmin}_{\theta} \mathcal{L}(\theta)$$

that define the optimal XC correlation functional. In the following scenario, we outline the use of a gradient-based method for training, although it should be noted that our approach is also compatible with gradient-free techniques, which would, however, prevent regularization as in ref. 25.

At each converged SCF calculation, the gradient of loss  $\mathcal{L}$  is performed via the automatic differentiation (or potentially parameter-shift rule on a quantum device). The gradient is then provided to the classical optimizer (Adam<sup>84</sup> or L-BFGS-B<sup>85</sup>). The learning rate for the Adam optimizer can be decreased from  $10^{-2}$  to  $10^{-4}$  as the training progresses to fine-tune the results. Otherwise, L-BFGS-B and Adam are used with the standard hyperparameters. To converge the training, it is possible to use a combination of Adam at first to ensure the escape of local minima due to the stochastic direction of the gradient in Adam and then switch to L-BFGS-B to follow the actual gradient, in order to achieve accurate results.

#### IV. RESULTS AND DISCUSSION

In this section, we present the outcomes of numerical experiments and comment on their performance in 1D and 3D settings. First, we evaluate all our models on  $\text{H}_2$  using the 1D KS-DFT framework. Next, we extend our approach to the 3D framework and test the extrapolation capacity of our models on the  $\text{H}_2$  molecule. We assess the effect of the fractional orbital occupation on  $\text{H}_2$  and evaluate our best model on planar  $\text{H}_4$ . We evaluate

the generalization capability on the  $\text{H}_2\text{H}_2$  system, which was not part of the training dataset, in a 1D setting. Finally, we estimate the number of measurements required in a quantum hardware implementation. All calculations are performed on a classical computer using Qadence.<sup>86</sup> For all our results, we define the density error in terms of the mean squared error (MSE) and include the local-density approximation (LDA) functional to contrast with our ML-based functionals. The hyperparameter search is performed for all proposed models and the best parameter combination (e.g., number of qubits  $N_q$ , layers  $N_l$  and depth  $N_d$ ) is selected.

##### A. Local versus global functionals

In Figure 3, we evaluate all our models within the 1D framework. This figure compares the prediction of 1D potential energy surfaces achieved by different models, characterizing the  $\text{H}-\text{H}$  bond dissociation in the  $\text{H}_2$  molecule. We start with MLP, which is the prototypical expressive model that we use to evaluate the approaches of local and global embeddings. To that end, in all our MLP models, we used 2 hidden layers with 513 neurons, which matches the number of grid points, to achieve enough expressivity. The Local MLP model has a single input and output neuron to infer the local XC energy based on corresponding density. Local MLP improves on the LDA DFT results in terms of overall energy error, but it is not sufficient to improve on the density. The restriction local information is limiting the capacity of the model to improve. Hence, we observe the best trade-off of energy-density error that this model is capable of.

In order to evaluate if local quantum models can improve on the Local MLP, we propose the Local ChQNN and PrQNN. These models employ the Chebyshev and product feature maps (see Appendix C), respectively. We use  $N_q = 4$  qubits,  $N_l = 1$  (no data reuploading) and  $N_d = 8$  layers for our ansatz. The results in terms of non-parallelity error (NPE) of the energy are very similar to those of the Local MLP model. The energy and density profiles of local quantum and classical models are qualitatively similar, as expected due to locality of both models. It is therefore necessary to verify if including more information in the quantum models brings benefits in terms of lower energy error  $|\Delta E|$  and MSE of the density profile.

For that purpose, we evaluate a global version of MLP with  $N_{\text{grid}} = 513$  input neurons. This allows the model to consider the whole density to infer the XC energy via the global embedding, hence there is only one output neuron. This results in  $\sim 2.6 \cdot 10^5$  parameters as reported in Table I. The corresponding energy profile is significantly improved (lower error with respect to the reference) in comparison to all other models. Similarly, the proposed KSR model<sup>25</sup> can be tailored to any locality. The global version of KSR model was shown to perform best and generalize perfectly in a single molecule even from only 2

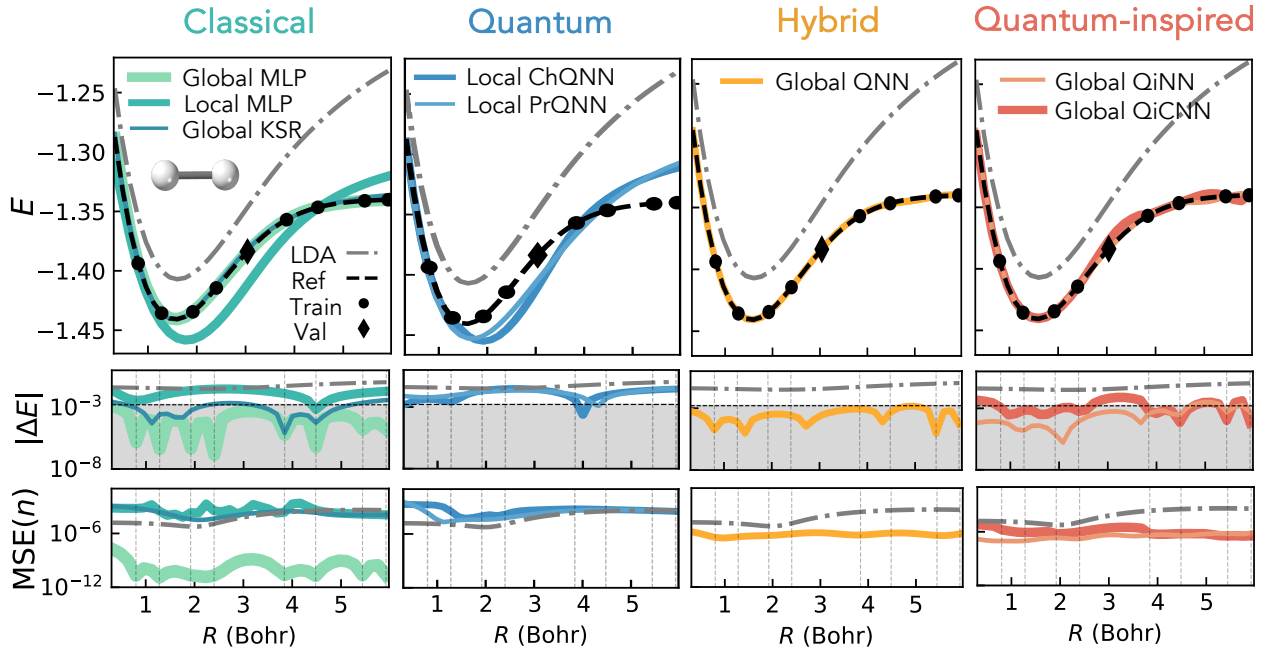


FIG. 3. Results of training neural XC functionals on different geometries of hydrogen molecule in 1D KS-DFT framework<sup>25</sup>. The grey area highlights results within chemical precision ( $\leq 1.6$  mHa) and vertical dashed lines mark the training data. Local models improve upon the LDA shape, but still produce a poor qualitative agreement with the reference. Best results are obtained for global models when the whole density is considered as model input. The XC models are defined in Section II C. All neural functionals are trained on eight training data points (circles) and the final model parameters are selected according to the lowest loss on the validation results. The reference (Ref) results are generated using DMRG by Li *et al.*<sup>25</sup>

TABLE I. Extrapolation results of neural XC functionals evaluated on H<sub>2</sub> within 1D KS-DFT framework (Fig. 3). Average energy and density errors, as well as non-parallelity error (NPE), are evaluated along the whole dissociation profile. The uncertainties were calculated using the standard deviation. For MLP-based models, we indicate the number of neurons per layer and the number of layers (e.g., 513/2). Description of the abbreviations: No.: number, Av.: average.

	Global MLP	Local MLP	Global KSR	Local ChQNN	Local PrQNN	Global QNN	Global QiNN	Global QiCNN
	$N_q/N_d/N_l$ 513/2	513/1	—	4/8/1	4/8/1	6/8/1	9/10/1	6/8/1
H <sub>2</sub>	No. parameters $2.64 \cdot 10^5$	1540	1568	96	108	144	297	596
	Avg. $ \Delta E $ [mHa] $(2 \pm 2) \cdot 10^{-4}$	$(1.5 \pm 0.9) \cdot 10^{-2}$	$(1 \pm 1) \cdot 10^{-3}$	$(1.5 \pm 1) \cdot 10^{-2}$	$(1.4 \pm 0.8) \cdot 10^{-2}$	$(4 \pm 4) \cdot 10^{-4}$	$(8 \pm 8) \cdot 10^{-4}$	$(3 \pm 2) \cdot 10^{-4}$
	NPE [mHa] $1.3 \cdot 10^{-3}$	$2.9 \cdot 10^{-2}$	$4 \cdot 10^{-3}$	$3.1 \cdot 10^{-2}$	$3.1 \cdot 10^{-2}$	$1.4 \cdot 10^{-3}$	$4 \cdot 10^{-3}$	$7 \cdot 10^{-4}$
	Avg. MSE(n) $(1.0 \pm 3.0) \cdot 10^{-9}$	$(5.6 \pm 6.0) \cdot 10^{-4}$	$(2.4 \pm 2.4) \cdot 10^{-4}$	$(6.0 \pm 5.3) \cdot 10^{-4}$	$(4.0 \pm 6.0) \cdot 10^{-4}$	$(7.2 \pm 2.4) \cdot 10^{-7}$	$(2.5 \pm 1.8) \cdot 10^{-3}$	$(2.1 \pm 1.0) \cdot 10^{-7}$

data points (here 8). We used the same density initialization as for Global MLP and the model struggled to generalize correctly, leading to MSE on density comparable to LDA, despite rendering chemically accurate energies. However, KSR is significantly more parameter-efficient, having only  $\sim 10^3$  parameters versus  $\sim 2.6 \cdot 10^5$  for Global MLP, which are generally known to overfit the training data. In addition, given good initialization, global KSR is capable of learning the dissociation profile of H<sub>2</sub> perfectly only from 2 data points, as shown in ref. 25. For all the remaining models with global embedding, the results perform as well or even better than local LDA-like functionals, at least for the total energies. Moreover, the global models have the lowest non-parallelity error (NPE) by an order of magnitude in comparison to local models (see Tab. I). A significant reduction (3-5 orders of magnitude) in average MSE of the electron density is achieved only by fully global models such as Global QNN and Global MLP.

Our results indicate that both classical and quantum models must incorporate global electron density features to achieve chemical precision.

## B. Extrapolation within a single molecule

All our models provide smooth energy profiles due to regularization capabilities of the employed differentiable DFT implementation. In Fig. 3, it is clear that 8 training data points, sampling low to strongly correlated regimes of the hydrogen molecule, are sufficient to generalize correctly within a single molecule, provided the model has enough expressivity. In general, all the models show characteristic dips in energy errors at the training data points. However, the density MSE profiles are rather flat along the whole dissociation curve. Similarly, in both Figs. 4 and 5, just 3 training points were sufficient to train models that provide qualitatively

correct energy profiles, even in the presence of strong correlation. Further studies are necessary to investigate the extrapolation capabilities of quantum models on large datasets, i.e., examining whether models trained only in strongly correlated regimes can extrapolate correctly to low-correlation regimes, and vice versa.

### C. Hybrid and quantum-inspired quantum-classical models

Since local QNNs are not capable of correctly fitting even the training data, we explore architectures that allow us to embed  $L$  data points and hence approach non-local functionals. In particular, in the Global QNN model, we consider the idea of embedding  $L$  data points in a single QNN with  $N_q = 6$  qubits,  $N_l = 1$  (no data reuploading) and  $N_d = 8$  layers, and apply the same model onto  $N_{\text{grid}}/L$  different batches. The results are combined via a single-layer MLP with 171 input neurons and 1 output for the global embedding. This allows us to embed chunks of data into a limited quantum model with a restricted number of qubits. By combining such outputs, we obtain a fully global functional. The model has only  $\sim 100$  trainable parameters, which is orders of magnitude smaller than for the Global MLP, since both are composed of most general quantum/classical layers. Note that comparing it with the KSR model is not reasonable because the latter possesses numerous inductive biases such as the self-interaction gate and the softly imposed negativity of XC energy.

We also evaluated the amplitude embedding as a feature map, using a DQC with  $N_q = 9$  qubits,  $N_l = 1$ ,  $N_d = 10$ . We name this model Global QiNN since, in general, it is hard to embed the classical data (electron density) exactly in a polynomial number of one-/two-qubit gates.<sup>87</sup> The number of qubits was chosen to fit all the elements of  $n$  exactly in a state-vector. In Tab. I, the results for Global QiNN are in good agreement with the reference: within chemical precision and overall density error that significantly improved upon LDA. Notably, the outcome is similar to Global QNN, which is simple to implement on near-term devices. The Global QiNN architecture, despite producing satisfactory results, does not produce a significant advantage over quantum-classical hybrid QNN. It can, however, serve for theoretical studies since only quantum layers are employed, which dissociates it completely from classical models.

Another approach is to chain quantum layers with angle embeddings, as implemented in the Global QiCNN model. In that case, the DQC output becomes the input of the next DQC layer. We use three different DQCs that all employ  $N_q = 6$  qubits,  $N_l = 1$  and  $N_d = 8$  ansatz layers. The third DQC layer feeds into an MLP layer with 19 neurons (remaining outputs of DQC at the third layer) to combine the results into the total XC energy. The results for the energy are within chemical precision. Concerning the density, the errors are significantly lower,

at least by an order of magnitude, than LDA.

Overall, among the hybrid quantum models presented, the simplest, Global QNN with a single quantum and classical layer, yields the best performance.

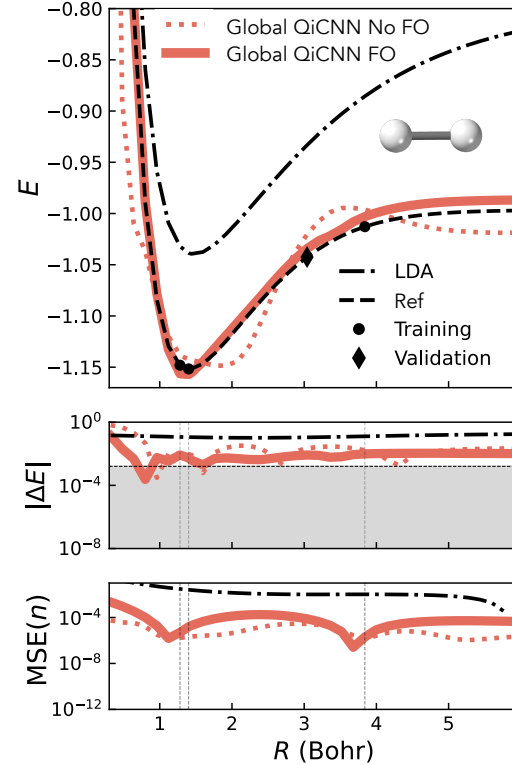


FIG. 4. Results of training neural XC functionals on different geometries of  $\text{H}_2$  in our 3D RKS-DFT framework based on PySCFAD. The same Global QiCNN (Eq. (19)) is trained with and without fractional orbital occupation (FO). Despite the limited training data (3 points), the model accurately extrapolates to distant geometries, demonstrating the strong regularization capacity of our 3D framework. The reference (Ref) results are generated using the FCI/6-31G level of theory.

TABLE II. Extrapolation results for Global QNN evaluated on  $\text{H}_2$  within 3D KS-DFT framework, both with and without fractional orbital occupation (FO) (Fig. 4).

	Global QiCNN No FO	Global QiCNN FO
$N_q/N_d/N_l$	4/14/1	4/14/1
No. parameters	653	653
$\text{H}_2$ Av. $ \Delta E $ [mHa]	$(5 \pm 13) \cdot 10^{-2}$	$(1 \pm 2) \cdot 10^{-2}$
NPE [mHa]	$6.5 \cdot 10^{-1}$	$1.3 \cdot 10^{-1}$
Av. $MSE(n)$	$(1.1 \pm 1.3) \cdot 10^{-5}$	$(1.5 \pm 3.7) \cdot 10^{-4}$

### D. Extension from 1D to 3D KS-DFT framework

To demonstrate the ability to efficiently train quantum XC models in our 3D framework, we evaluate our

most complex neural functional, Global QiCNN, in such a setting. Similarly to the 1D version, the model consists of 3 chained quantum layers, each with  $N_q = 4$  qubits,  $N_l = 1$  and  $N_d = 14$  ansatz layers. The final quantum layer connects to MLP with 149 neurons to output the total XC energy. As depicted in Fig. 4, Global QiCNN suffers from energy oscillations and is unable to extrapolate correctly. This is the ideal situation to demonstrate the ability of fractional occupation (FO) methods to alleviate such problems, which are apparent in 3D due to increased complexity. To that end, we show that even with 3 data points (of which 2 are almost at the same bond distance) the complex model can be regularized in order to fit better the dissociation curve, e.g., lower NPE (see Tab. II). Despite not being within chemical precision along the whole energy profile, the density error is improved by orders of magnitude in comparison to the LDA result. This is achieved with a FO algorithm<sup>81</sup> that is discussed in Appendix A. The FO approach relaxes the constraint of the integer orbital occupation in PySCF's restricted KS-DFT implementation and allows us to approximate the true fractional ones. In addition, the neural XC functional is optimized through training, thereby compensating for errors arising from the approximation of orbital occupations. As reported in Tab. II, the use of the FO approach results in an approximately 5-fold reduction in both the average energy error and its variance, without any extra model parameters. Note that the FO method is not limited to use only with quantum models; it can also be applied more broadly for training classical neural XC functionals.

As the ultimate test of our 3D framework, demonstrating the capability to accurately learn from challenging molecular systems, we trained our best hybrid architecture, the Global QNN, on planar H<sub>4</sub>. This is a typical small system exhibiting strong correlation, commonly used to benchmark *ab initio* methods.<sup>88,89</sup> Here, Global QNN consists of one quantum layer with  $N_q = 4$  qubits,  $N_l = 1$ ,  $N_d = 14$  and followed by MLP with 596 neurons that outputs  $E_{XC}$ . In Fig. 5, we note that even after the shift, the LDA approximation greatly overestimates the energy barrier at  $\beta = 90^\circ$ . This quantum-classical hybrid model, given its limited expressivity, provides the best achievable fit of the training data and extrapolates smoothly to various geometries. In Tab. III, we note that the model achieves chemical precision over the whole energy profile ( $NPE \approx 10^{-4}$ ). Concerning density errors, they are of the order of  $10^{-5}$ , similar to the H<sub>2</sub> density errors (Tab. II) that are obtained within the same 3D framework. Hence, we demonstrated that provided accurate reference data, it is possible to train quantum-enhanced functionals to learn from strongly correlated systems. In the future, it would be interesting to evaluate if such models can generalize correctly from small to other larger strongly correlated systems such as stretched N<sub>2</sub>.

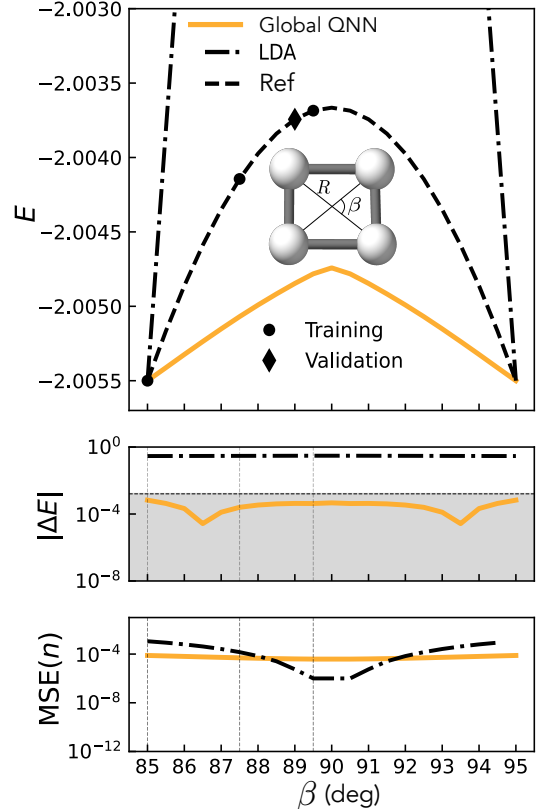


FIG. 5. Extrapolation of Global QNN (Eq. (15)) on planar H<sub>4</sub> within the 3D framework with a fractional occupation approach.<sup>81</sup> Global QNN achieves chemical precision in energy, surpassing the LDA results by orders of magnitude. In the top panel, LDA and Global QNN results are shifted to match the reference data at extremities to compare the shapes of the dissociation profiles. Shifts can be inferred from the  $|\Delta E|$  panel. The reference (Ref) results are generated with the FCI/6-31G level of theory.

TABLE III. Extrapolation results for Global QNN evaluated on H<sub>4</sub> within the 3D KS-DFT framework (Fig. 5).

	Global QNN
$N_q/N_d/N_l$	4/14/1
No. parameters	764
H <sub>4</sub>	
Av. $ \Delta E $ [mHa]	$(3 \pm 2) \cdot 10^{-4}$
NPE [mHa]	$6 \cdot 10^{-4}$
Av. MSE( $n$ )	$(5.3 \pm 1.2) \cdot 10^{-5}$

### E. Zero-shot generalization of XC functionals

In Fig. 3, we demonstrated that quantum-enhanced XC models can learn to extrapolate correctly to different geometries of a single molecule by consistently achieving chemical precision within the 1D framework. To evaluate their capacity to generalize to different molecular systems, we select our best-performing quantum-enhanced functional and test it on a molecular system that was not included in the training dataset.

Our results highlight Global QNN as the simplest hy-

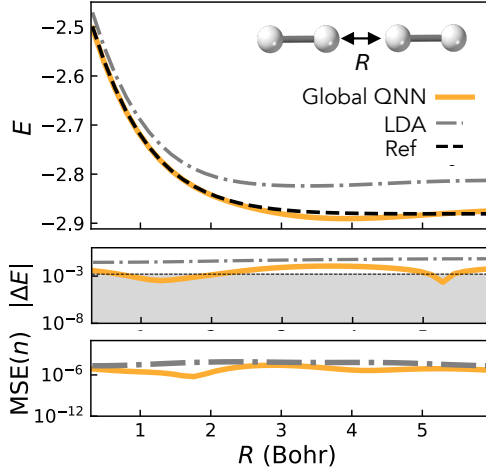


FIG. 6. Generalization of Global QNN (Eq. (15)) to unseen  $\text{H}_2\text{H}_2$  system trained on  $\text{H}_2$  and  $\text{H}_4$  molecules within the 1D framework. The model achieves chemical precision over some regions of the dissociation profile without being explicitly trained on it. The reference (Ref) results are generated using DMRG by Li *et al.*<sup>25</sup>

brid model, comprising a single quantum and classical layer, capable of achieving chemical precision for  $\text{H}_2$ . For its training, the dataset only contained the hydrogen molecule at different geometries. Such a dataset does not allow the model to implicitly learn the XC energy dependency on the variable number of electrons  $N_e$  in the input density (i.e.,  $N_e = \sum_{i=1}^{N_{\text{grid}}} w_i n_i$ ) when evaluating on a different system such as  $\text{H}_2\text{H}_2$  (separate hydrogen molecules). Hence, we enrich our train dataset with molecules such as linear  $\text{H}_4$  at different bond distances, as done in ref.<sup>25</sup> We train Global QNN using the following bond distances: For  $\text{H}_2$ ,  $R \in (0.48, 1.28, 3.04, 3.84)$  Bohr and for  $\text{H}_4$ ,  $R \in (1.28, 2.08, 3.36, 4.48)$  Bohr.

In Fig. 6, we note that chemical precision is achieved only for small values of  $R < 2$  Bohr and momentarily at  $R = 5.3$  Bohr, with the overall energy closely aligned with the reference, resulting in lower energy error compared to LDA. MSE on the density consistently remains lower than the LDA result. The XC model yields sub-optimal qualitative predictions, evidenced by the energy minimum at approximately 3.5 Bohr (stable configuration). Considering the utilization of only basic classical and quantum layers and a few data points, these results demonstrate the capacity of our models to generalize. In fact, as stated in Tab. IV, our model has only 144 trainable parameters compared to the state-of-the-art Global KSR model, which has 10 times more. Hence, addressing the shortcomings would require improving the architecture of our model (e.g., using molecular symmetries) and expanding the training dataset, which is beyond the scope of this study.

TABLE IV. Zero-shot generalization results for Global QNN evaluated on  $\text{H}_2\text{H}_2$ , trained on  $\text{H}_2$  and  $\text{H}_4$  within the 1D KS-DFT framework (Fig. 6).

		Global QNN
	$N_g/N_d/N_l$	6/8/1
	No. parameters	144
$\text{H}_2\text{H}_2$	Av. $ \Delta E $ [mHa]	$(4.9 \pm 1.4) \cdot 10^{-2}$
	NPE [mHa]	$3.9 \cdot 10^{-2}$
	Av. MSE( $n$ )	$(5 \pm 2) \cdot 10^{-5}$

#### F. Resource estimations for quantum hardware implementation

A robust evaluation of a competitive quantum model ideally involves assessing its time-to-solution, generalization capacity, parameter efficiency, and expressive power. In this context, the resources required for evaluating quantum XC models align with those conventionally utilized for DQC-based QNNs.<sup>36</sup> We focus on the time-to-solution, which is contingent on the total number of measurements (shots) required for an accurate output evaluation of quantum models. To that end, we examine the number of shots needed for the gradients  $\nabla_\theta E_{\text{XC}}$ ,  $v_{\text{XC}}[n](\mathbf{r}) = \delta E_{\text{XC}}[n]/\delta n(\mathbf{r})$  and energy  $E_{\text{XC}}$  evaluations during the training phase.

For a single gradient evaluation, the cost operator  $\hat{C} = \sum_{i=1}^{N_q} \hat{Z}_i$ , in the loss function is diagonal by design. It allows for the simultaneous measurement of all its terms (due to mutual commutation), thereby mitigating associated errors on noisy quantum processors. This drastically reduces the number of shots in comparison to common *ab initio* variational approaches<sup>90,91</sup> that require the cost operator to be the electronic Hamiltonian of given system, which typically has many non-commuting terms to be measured (i.e.,  $\mathcal{O}(N^4)$  terms, where  $N$  is the system size). To evaluate  $\nabla_\theta E_{\text{XC}}$  or  $v_{\text{XC}}$  by using the parameter-shift rule<sup>39</sup>, two expectation values need to be computed at each epoch during the training (see Appendix D). In practical terms, considering that we have  $N_{\text{epochs}}$  during training, we require  $N_{\text{shots}}$  per expectation value to achieve the desired accuracy  $\epsilon_{\text{exp}}$ . Consequently, the total number of shots during training performed for  $\nabla_\theta E_{\text{XC}}$ , taking into account  $N_{\text{param}}$  training parameters, amounts to  $2N_{\text{shots}}N_{\text{param}}N_{\text{epochs}}$ . Similarly for  $v_{\text{XC}}$ , the gradient  $\delta E_{\text{XC}}[n]/\delta n(\mathbf{r})$  is evaluated at  $N_{\text{grid}}$  points, resulting in  $2N_{\text{shots}}N_{\text{grid}}N_{\text{epochs}}$  shots.

In addition,  $E_{\text{XC}}$  needs to be inferred at every KS iteration. In our experience, the number of KS iterations can be set at  $N_{\text{KS}} \in [15 - 100]$  depending on the size and complexity (strongly correlated regime) of the system. The total cost in terms of measurements is given by  $(2N_{\text{param}} + 2N_{\text{grid}} + N_{\text{KS}})N_{\text{shots}}N_{\text{epochs}}$ . We consider the number of trainable parameters  $N_{\text{param}}$  that is significantly larger than  $N_{\text{KS}}$  but smaller than the grid size  $N_{\text{grid}}$ , which scales linearly with the number of atoms  $N_{\text{grid}} \sim \mathcal{O}(N_{\text{atoms}})$ . Hence, the overall cost in terms of measurements is generally expected to scale as

$\mathcal{O}(N_{\text{shots}} N_{\text{grid}} N_{\text{epochs}}) \sim \mathcal{O}(N_{\text{atoms}})$ . This scaling is valid for the global energy embedding (Eq. (5)), a singular energy evaluation suffices ( $E_{\text{XC}}[n] \approx F_{\theta}[n]$ ).

In a local embedding scenario, the XC energy  $E_{\text{XC}}$  is approximated through  $N_{\text{grid}}$  model evaluations, where the total error is the weighted sum of individual errors, leading to number of shots much greater than with the global energy embedding,  $N_{\text{grid}} N_{\text{KS}} N_{\text{shots}} N_{\text{epochs}} \gg N_{\text{KS}} N_{\text{shots}} N_{\text{epochs}}$ . Hence, the number of expectation values is  $(2N_{\text{param}} + 2N_{\text{grid}} + N_{\text{grid}} N_{\text{KS}}) N_{\text{shots}} N_{\text{epochs}}$ . In terms of scaling with the system size, consider the model fixed (number of parameters is constant) and  $N_{\text{grid}} \sim \mathcal{O}(N_{\text{atoms}})$ . Then, the number of measurements scales with the system size as  $\mathcal{O}(N_{\text{atoms}})$ .

TABLE V. Scaling of the number of measurements for the training with the proposed local (Eq. (4)) and global (Eq. (5)) energy embeddings in quantum-enhanced KS-DFT.

	Local	Global
$E_{\text{XC}}$	$\mathcal{O}(N_{\text{shots}} N_{\text{grid}} N_{\text{epochs}})$	$\mathcal{O}(N_{\text{shots}} N_{\text{epochs}})$
$\nabla_{\theta} E_{\text{XC}}$	$\mathcal{O}(N_{\text{shots}} N_{\text{param}} N_{\text{epochs}})$	$\mathcal{O}(N_{\text{shots}} N_{\text{param}} N_{\text{epochs}})$
$v_{\text{XC}}$	$\mathcal{O}(N_{\text{shots}} N_{\text{grid}} N_{\text{epochs}})$	$\mathcal{O}(N_{\text{shots}} N_{\text{grid}} N_{\text{epochs}})$
Total	$\mathcal{O}(N_{\text{grid}}) \sim \mathcal{O}(N_{\text{atoms}})$	$\mathcal{O}(N_{\text{grid}}) \sim \mathcal{O}(N_{\text{atoms}})$

Thus, the total cost for training with local or global energy embedding scales linearly with the system size in terms of shots due to the need to evaluate the local XC potential on the grid. The aforementioned costs are summarized in Table V. On quantum hardware, the overall time required for training quantum models depends on the single-shot rate, highly dependent on the hardware type. This consideration ultimately determines the computational resources needed to attain a practical advantage (e.g., lower inference time) over classical XC models.

Given the imperative to consistently achieve chemical precision for meaningful outcomes (e.g., accurate energy barriers), global embedding of the quantum XC functional (see Eq. (5)) emerges as the most promising near-term approach (i.e., especially in situations with small grid size,  $N_{\text{grid}} \ll N_{\text{shots}}$  and  $N_{\text{grid}} \ll N_{\text{epochs}}$ ). In our experiments, as our loss function is defined against energies, the fact that the global energy embedding does not scale with grid size significantly reduces the energy error of our models in comparison to the local embedding, leading to the best outcomes.

## V. CONCLUSIONS AND OUTLOOK

In this work, we developed various (Q)NN-based architectures and evaluated their capabilities to represent XC functionals within KS-DFT. To that end, we extended existing differentiable KS-DFT codes based on JAX and PySCF frameworks, in both 1D and 3D settings, to accommodate quantum models. Next, we defined four classes of models capable of incorporating an arbitrary number of quantum and/or classical layers. As

in other works,<sup>25,28</sup> we classified the models by their locality (i.e., the fraction of density points considered as the input). To integrate these architectures into KS-DFT, we introduced a global embedding strategy, well suited for quantum architectures due to its minimal measurement requirements on quantum hardware. In terms of scalability, both local and global approaches are influenced by the system size due to the need to compute the local XC potential. However, a significant advantage of our model is that the global energy embedding does not scale with the grid size. This feature substantially improved the accuracy of our model, yielding the best results in our experiments. Finally, we performed numerical simulations of the entire training process on a classical computer.

The results of our experiments demonstrate the promising capabilities of QNNs in efficiently modelling the XC energy functionals and doing so with potentially fewer training parameters due to greater expressivity compared to classical NNs<sup>37</sup>, with theoretical arguments outlined in Sec. IID. Only fully global (quantum-enhanced) models, where the whole density is considered, produced the best results. In particular, Global QNN provided the simplest, yet sufficiently expressive architecture to model with chemical precision the small molecular systems considered in this work, both in 1D ( $H_2$ ) and 3D (planar  $H_4$ ), even in the presence of strong correlation. With a mere 144 trainable parameters, Global QNN produced similar results to the state-of-the-art Global KSR model, which requires ten times more parameters. The same modest model demonstrated satisfactory generalization capability on the  $H_2H_2$  system (two separate hydrogen molecules), despite being trained solely on  $H_2$  and  $H_4$ . This offers a promising perspective on the potential of QNNs for generalization within this framework. Moreover, we incorporated a fractional orbital occupation approach into our framework, which can be also employed to train purely classical models. This FO approach was instrumental in enhancing the accuracy of our models in 3D. By employing the FO method, we reduced both the average energy error and its variance by approximately six-fold. In that way, we effectively mitigated energy oscillations and substantially improved the extrapolation accuracy of Global QiCNN. Additionally, in our QML approach, a quantum-enhanced neural functional can be initially trained and subsequently fine-tuned with additional data as needed. Once trained, this functional can be directly applied to any system to infer its properties. This stands in contrast to variational quantum eigensolver<sup>90</sup> and imaginary time<sup>91</sup> approaches, which necessitate full optimization for each system. The latter methods evolve the quantum state using the exact electronic Hamiltonian. In contrast, QML methods depend on the quality of the training data to ensure qualitatively correct predictions.

As an outlook, in this study, we provided an initial evaluation of proposed techniques on quantum/classical neural architectures and molecules. In future works, it would be necessary to expand our training dataset

substantially to understand the practical efficiency of quantum-enhanced models. Efforts to construct such datasets are currently ongoing.<sup>32</sup> The capability of our models to generalize to significantly larger systems is a critical aspect to investigate. Specifically, can these models effectively learn from small, strongly correlated systems and subsequently generalize accurately to larger systems? In our implementation, we were limited in the efficiency of our code, which requires further optimizations to enable large-scale training.

The FO approach<sup>81</sup> employed in this study has been evaluated solely on dimers. It remains to be verified whether a single value of the temperature parameter  $\gamma$ , as detailed in Appendix A, is adequate for training on larger datasets. Alternatively, parameter-free FO approaches, such as the quadratically convergent method can be employed instead<sup>82</sup>. In this work, we opted for the simplest-to-implement method.

Moreover, the practicality of our approach is limited by significant overhead in shots, since the training requires not only the ansatz parameter derivatives but also the feature map differentiation for the XC potential. The training cannot be performed in a gradient-free manner without losing the regularization provided by differentiating through the KS iterations. Only quantum hardware that may achieve high shot rate would make this approach practical, since accurate gradients are necessary. Additionally, the impact of noise in expectation values when using the parameter-shift rule during the training of quantum models needs to be assessed. However, model architectures that utilize quantum computers without their direct optimization on a QPU, may provide the solution to the aforementioned problems. Since electron density on a grid can be viewed as a graph, graph-based models present interesting alternatives. Recently, a quantum-enhanced graph transformer model was shown to exhibit a provable advantage in expressivity for specific families of graphs.<sup>92</sup> Only the classical layers necessitate differentiation, with the quantum computer solely employed to extract relevant graph features. Such models would be particularly suited for the learning of XC functionals on PASQAL's neutral atom QPUs, which provide additional capabilities of analog quantum computing.

As possible future research directions, concerning the gate-based models studied in this work, we can consider introducing trainable feature maps<sup>93</sup> to improve the accuracy by increasing expressivity at the cost of extra variational parameters. Symmetries can be incorporated into quantum layers to enforce XC energy invariance with respect to these symmetry operations (e.g., rotations, reflections), hence improving generalization capabilities of quantum models.<sup>62</sup> The QNN formulation can be directly swapped for kernel-based approaches<sup>94</sup> that model the XC functional as  $f_\theta(n) = b + \sum_{i=1}^{|D|} \alpha_i \kappa_\theta(n, n_{\text{ref}}^i)$ , where  $\kappa_\theta(n, n_{\text{ref}}^i) = |\langle \phi_\theta(n) | \psi(n_{\text{ref}}^i) \rangle|^2$  is the trainable kernel that computes the overlap between the quantum states corresponding to input data,  $|\phi_\theta(n)\rangle$ , and reference data embedding,  $|\psi(n_{\text{ref}}^i)\rangle$ . Among the train-

able parameters, the scalar  $b$  represents the offset and  $\alpha$  coefficients weigh the combinations of different kernels. To produce the mapping of the density to the Hilbert space,  $|\phi_\theta(n)\rangle$ , standard digital circuits or analog circuits<sup>95</sup> can be used. To map the reference density, Chebyshev and product feature maps can be employed, as in this work. The kernel approach is particularly suitable for the implementation on neutral atom-based devices via the quantum evolution kernel,<sup>96</sup> where the reference and input data can be written into Hamiltonian coefficients. Finally, in the fault-tolerant era, it would be possible to represent the XC functional as an overlap,  $f_\theta(n) = \langle \phi(n) | \psi_\theta \rangle$ , via the amplitude-based Fourier, Chebyshev encodings for  $|\phi(n)\rangle$  and differentiation rules proposed in ref.<sup>97</sup> Standard DQCs can be employed for representing  $|\psi_\theta\rangle = U(\theta)|0\rangle$  and the same loss functions can be used for its training, as in this work. The use of amplitude data encodings proposed in ref.<sup>97</sup> would take advantage of exponentially many independent basis functions, further increasing the expressivity of quantum-based XC models, potentially making possible the representation of the universal XC functional.

Overall, our findings emphasize the promising potential of QNN/kernel-based XC functionals within DFT. With this contribution, we provided an initial blueprint that would serve as a stepping stone towards the development of more optimized frameworks and quantum-enhanced neural architectures that can tackle even more challenging chemical problems with greater accuracy and efficiency.

## VI. ACKNOWLEDGEMENTS

The authors thank the PASQAL team for fruitful discussions, especially Atiyo Ghosh, Andrea A. Gentile and Louis-Paul Henry for their valuable insights.

## Appendix A: Incorporating fractional occupation in RKS-DFT

Chai's algorithm for fractional occupation is based on the argument that the distribution of occupation numbers is independent of the specific many-body system and adheres to a universal form described by the Fermi-Dirac distribution.<sup>81</sup> Hence, the density can be expressed as  $n(\mathbf{r}) = \sum_{i=1}^{\infty} g_i |\psi_i(\mathbf{r})|^2$ , where the occupation number  $g_i$  is the Fermi-Dirac function  $g_i = \{1 + \exp[(\epsilon_i - \mu)/\gamma]\}^{-1}$ , which obeys the following two conditions,  $\sum_{i=1}^{\infty} g_i = N$ , and  $0 \leq g_i \leq 1$ , where  $\epsilon_i$  is the orbital energy of the  $i^{\text{th}}$  orbital  $\psi_i(\mathbf{r})$ , and  $\mu$  is the chemical potential chosen to maintain a constant number of electrons  $N$ . To account for this modification, the expression for the energy

is then given by

$$E[n] = T_s^\gamma [\{g_i, \psi_i\}] - \frac{\gamma}{k_B} S[\{g_i\}] + \int n(\mathbf{r})v(\mathbf{r})d\mathbf{r} \quad (\text{A1})$$

$$+ E_H[n] + E_{XC}^\gamma[n].$$

with  $\gamma$ -dependent XC energy given by  $E_{XC}^\gamma[n] = E_{XC}[n] + E_\gamma[n]$ , where  $E_\gamma[n]$  represents the difference between the non-interacting kinetic free energy at zero temperature and that at temperature  $\gamma$ . The entropy contribution is given by  $-\frac{\gamma}{k_B} S_s^\gamma [\{g_i\}] = \gamma \sum_{i=1}^{\infty} [g_i \ln(g_i) + (1-g_i) \ln(1-g_i)]$ . Given a suitable electronic temperature  $\gamma$ , the chemical potential  $\mu$  is fixed by  $\sum_{i=1}^{\infty} \{1 + \exp[(\epsilon_i - \mu)/\gamma]\}^{-1} = N$  to conserve the number of particles. In essence, only the entropy contribution needs to be added to an existing RKS-DFT implementation and  $E_{XC}^\gamma[n]$  is learned by the neural XC. This approach does not impact the overall computational scaling. The trade-off for improved density representability is the inclusion of a single free parameter, the temperature  $\gamma$ , which may require initial tuning for consistency across systems, a subject that warrants further investigation.

## Appendix B: Integration grids and neural XC functionals

A neural XC model needs to implicitly learn a function  $f_\theta$  that is adapted to the  $\{w_i\}_{i=1}^{N_{\text{grid}}}$  grid points, distributed according to a fixed grid type. There are multiple choices of grid types and densities (number of grid points  $N_{\text{grid}}$ ), with a finer grid mesh yielding more accurate results at a higher computational cost. Ideally, a neural XC model needs to be trained/constrained to be invariant to finer mesh grids of the same type. See Fig. 7 where a trained Global QNN model is used to compute the electron density throughout KS iterations on a fixed grid of 513 points. This adds to the challenge of making generalizable neural XC functionals where grid (hence the number of model inputs) needs to be adapted and neural XC functional made consistent with the changes. For instance, a potential solution is to design a grid invariant embedding or add constraints in the loss to make the NN  $f_\theta$  invariant to grid density changes. Another approach would be to use also the coordinates  $\{\mathbf{r}_i\}_{i=1}^{N_{\text{grid}}}$  as inputs of the model  $f_\theta$  to explicitly include the information about the distribution of grid points in the Cartesian space. However, this approach would quadruple the number of inputs, so it is not currently considered for simplicity. In our work, we minimize grid variations by using a single grid type (e.g., of Lebedev type<sup>98</sup>) and the same number of grid points for all molecules whenever possible (our models have a fixed number of  $N_{\text{grid}}$  inputs) in order to facilitate the training.

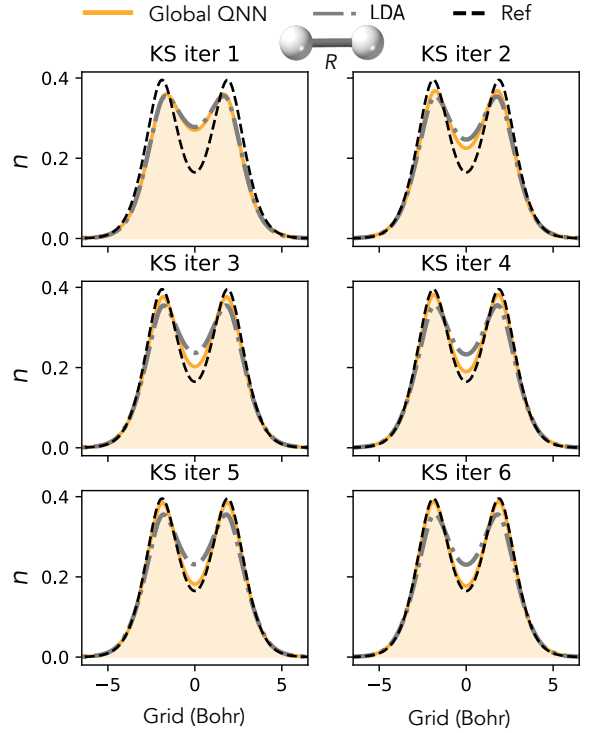


FIG. 7. Electron density of a hydrogen molecule ( $R = 3.84$  Bohr) at first six KS iterations using Global QNN within the 1D KS-DFT framework. At every KS iteration, the electron density is improved, eventually reaching the reference one. The reference (Ref) result is generated using DMRG by Li *et al.*<sup>25</sup>.

## Appendix C: Building blocks of quantum neural networks

In this section, we present typical differentiable quantum circuits (DQCs) that are used in this work.

### 1. Quantum circuit ansatz

As an ansatz  $U_a$  layer, we employ the popular Hardware-Efficient Ansatz (HEA) introduced in the context of VQE for chemistry.<sup>90</sup> The heuristic ansatz structure is not specifically tailored to the problem; thus, it represents the most general quantum model, closely resembling a classical MLP. It is composed of selected single qubit rotations (i.e.,  $R_z(\theta) = e^{-\frac{i}{2}\theta\hat{Z}}$ ) that are placed on all available qubits with distinct angles  $\theta_a$ ,

$$U_{\text{sqr}}(\theta_a) = \prod_{i=1}^{N_q} e^{-\frac{i}{2}\theta_{a,x}^i \hat{Z}} e^{-\frac{i}{2}\theta_{a,y}^i \hat{X}} e^{-\frac{i}{2}\theta_{a,z}^i \hat{Z}}, \quad (\text{C1})$$

which enables the representation of the most general rotation on a Bloch sphere. The entanglement block consists of an arbitrary pattern of (parameterized) multi-qubit gates that introduce interactions between qubits.

For example, considering the two-qubit case, a unitary is given by

$$U_{\text{ent}} = \prod_{(i,j) \in S} \text{CNOT}(i,j) \quad (\text{C2})$$

where  $\text{CNOT}(i,j) = e^{-\frac{i}{4}(I_i - \hat{Z}_i)(I_j - \hat{X}_j)}$  and  $S$  represents an ordered set of pairs of qubit indices. We will employ an “alternate ladder” set  $S_{\text{al}} = S_1 \cup S_2$  with  $S_1 = ((0,1), (2,3), \dots, (N_q-1, N_q))$  and  $S_2 = ((1,2), (3,4), \dots, (N_q-2, N_q-1))$  unless specified otherwise. Note that a parametrized entanglement layer can also be defined as  $U_{\text{ent}}^{\text{RZZ}}(\theta_{\text{ent}}) = \prod_{(i,j) \in S} R_{\text{ZZ}}^{i,j}(\theta_{\text{ent}}) = \prod_{(i,j) \in S} \text{CNOT}(i,j) e^{-\frac{i}{2}\theta_{\text{ent}}^i \hat{Z}} \text{CNOT}(i,j)$ , where  $R_{\text{ZZ}}^{i,j}$  represents the parametrized ZZ gate between qubits. This allows the model to cancel the interaction ( $\theta_{\text{ent}}^{i,j} = 0$ ) between qubits if necessary. The final quantum state  $|\psi\rangle$  prepared by repetitive applications of the feature map and ansatz is given by

$$|\psi(n, \theta)\rangle = \prod_{l=0}^{N_l} \left( \prod_{d=0}^{N_d} U_{\text{ent}}^{l,d} U_{\text{sqr}}^{l,d}(\theta_a^{l,d}) U_f^l(n) \right) |0\rangle, \quad (\text{C3})$$

and subsequently used in Eq. (13) as  $f_\theta(n) = \langle \psi(n, \theta) | \hat{C} | \psi(n, \theta) \rangle$ . Throughout this work, all the quantum layers will be evaluated in this manner. Next, we discuss how classical data can be embedded in quantum circuits  $U_f(n)$ .

## 2. Feature maps

The choice of the feature map is crucial for the expressiveness of (quantum) XC functionals.<sup>44</sup> We consider encoding the data in the parameters (angles) of quantum circuits and directly into the amplitudes of computational basis states  $\{|i\rangle\}_{i=1}^{2^{N_q}}$ . The most general angle embeddings are specific cases of feature maps expressed as

$$U_f(\mathbf{n}) = \bigotimes_{k=1}^{N_{\text{grid}}} e^{-\frac{i}{2}\varphi(n_k) \hat{G}_k}, \quad (\text{C4})$$

with generators  $\hat{G}$  and a data transformation function  $\varphi : \mathbb{R} \rightarrow \mathbb{R}$ . Note that the generators can be multi-qubit operators. Concretely, we consider the following types: (i) *Product* (Pr) (ii) *Chebyshev* (Ch) for angle encodings and (iii) *Amplitude* data encodings.<sup>36</sup> These strategies are well-established methods for embedding the data in quantum circuits. Next, we explicitly give their definition.

## 3. 1-local product feature map

The fully local version (1-local) of the product feature map embeds the data value  $n_k$  in the rotation angles of

$R_y$  gates ( $\hat{G}_l = \hat{Y}_l$ ) of all qubits as

$$U_{f,\text{pr}}^{(1)}(n_k) = \bigotimes_{l=1}^{N_q} e^{-\frac{i}{2}n_k \hat{Y}_l}. \quad (\text{C5})$$

## 4. 1-local Chebyshev feature map

Another feature map, which utilizes an efficient polynomial basis, is the Chebyshev tower feature map. It was first introduced in ref. 36 and is defined by

$$U_{f,\text{ch}}^{(1)}(\mathbf{n}) = \bigotimes_{k=1}^{N_q} e^{-k \cdot \arccos(n_k) \hat{Y}_k}. \quad (\text{C6})$$

Despite its efficiency, the data normalization, e.g.,  $\mathbf{n} \rightarrow \frac{\mathbf{n}}{\|\mathbf{n}\|}$ , is required due to the domain definition of  $\arccos$  to  $[-1, 1]$ . This entails that the information about the number of electrons is lost, since the normalization would change for every chemical system. Normalizing by a fixed value is a limited solution, since, depending on the system, the rescaling might not be sufficient. Hence, this feature map is unsuitable for the models that take only into account the density as inputs, which is the case in this work.

## 5. L-local product feature map

Multiple data points can also be encoded by a single feature map. For this purpose, we define the  $L$ -local version of  $U_{f,\text{pr}}$  by embedding different data points into single qubit gates angles associated with available qubits,

$$U_{f,\text{pr}}^{(L)}(\mathbf{n}) = \bigotimes_{k=1}^L e^{-\frac{i}{2}n_k \hat{Y}_k}, \quad (\text{C7})$$

where  $L$  denotes the number of data points that are embedded in the circuit simultaneously. Note that since every feature map presented so far can embed at most  $1 \leq L \leq N_q$  data points, there are  $\lceil N_{\text{grid}} / L \rceil$  different embeddings for grid points to perform (model executions), which can be done in parallel since they are independent.

## 6. Global amplitude-based feature map

Lastly, we consider the mapping of the density vector  $\mathbf{n}$  to a quantum state as  $|\mathbf{n}\rangle = U_{f,a}^{(N_{\text{grid}})}(\mathbf{n})|0\rangle$ . Due to the unitary, the density is transformed as  $\mathbf{n} \rightarrow \frac{\mathbf{n}}{\|\mathbf{n}\|}$  to a unit vector prior to quantum embedding. This also suppresses information about the number of electrons that hinders the model’s performance. In general, there exists no efficient algorithm (i.e., that uses a polynomial number of gates) for implementing the unitary  $U_{f,a}^{(N_{\text{grid}})}(\mathbf{n})$

for an arbitrary vector  $\mathbf{n}$ .<sup>99</sup> Hence, we will consider this feature map only in our quantum-inspired models.

#### Appendix D: Differentiation of quantum models

Gradient evaluation is an essential component for training NNs in general. Since (quantum) NNs can be thought of as a function  $f_\theta$ , there are various approaches for differentiation. The standard approach in classical ML is the *Automatic Differentiation* (AD) that exploits the chain rule and stores the intermediate values of sub-functions (layers) of ML models to evaluate the gradients of  $f_\theta$ . This approach has an advantageous scaling that enables training large classical models and, hence, is always used for the differentiation of classical layers in this work.

In the context of quantum computing, there has been a need to develop an efficient approach, beyond finite differences, for gradient evaluation. Schuld *et al.* showed that due to the trigonometric relations within the unitaries associated with single qubit rotations,  $U_{\text{sqr}} = e^{-\frac{i}{2}\theta\hat{O}}$  (that include single-qubit Pauli generators  $\hat{O}$ ), it is possible to derive a simple and exact derivative formula which highly resembles finite differences, the so-called *Parameter-Shift Rule* (PSR):<sup>39</sup>

$$\nabla_\theta f_\theta(n) = \frac{f_{\theta+\pi/2}(n) - f_{\theta-\pi/2}(n)}{2}. \quad (\text{D1})$$

The generalized PSR (GPSR) rule<sup>40</sup> is needed for general multi-qubit generators.

\* [sokolov.igor.ch@gmail.com](mailto:sokolov.igor.ch@gmail.com)

- <sup>1</sup> R. G. Parr and W. Yang, *Density-Functional Theory of Atoms and Molecules*, International Series of Monographs on Chemistry (Oxford University Press, 1994).
- <sup>2</sup> W. Koch and M. C. Holthausen, *A Chemist's Guide to Density Functional Theory* (Wiley, 2015).
- <sup>3</sup> E. Engel and R. M. Dreizler, *Density Functional Theory: An Advanced Course*, Theoretical and Mathematical Physics (Springer Berlin Heidelberg, 2011).
- <sup>4</sup> A. D. Becke, J. Chem. Phys. **140**, 18A301 (2014).
- <sup>5</sup> R. O. Jones, Rev. Mod. Phys. **87**, 897.
- <sup>6</sup> A. J. Cohen, P. Mori-Sánchez, and W. Yang, Chem. Rev. **112**, 289 (2012).
- <sup>7</sup> M. G. Medvedev, I. S. Bushmarinov, J. Sun, J. P. Perdew, and K. A. Lyssenko, Science **355**, 49 (2017).
- <sup>8</sup> K. P. Kepp, Science **356**, 496 (2017).
- <sup>9</sup> A. J. Cohen, P. Mori-Sánchez, and W. Yang, Science **321**, 792 (2008).
- <sup>10</sup> A. J. Cohen, P. Mori-Sánchez, and W. Yang, J. Chem. Phys. **129** (2008).
- <sup>11</sup> A. D. Becke, J. Chem. Phys. **140** (2014).
- <sup>12</sup> N. Mardirossian and M. Head-Gordon, Molecular Physics **115**, 2315 (2017).
- <sup>13</sup> L. Goerigk, A. Hansen, C. Bauer, S. Ehrlich, A. Najibi, and S. Grimme, Phys. Chem. Chem. Phys. **19**, 32184 (2017).
- <sup>14</sup> E. Caldeweyher, S. Ehlert, A. Hansen, H. Neugebauer, S. Spicher, C. Bannwarth, and S. Grimme, J. Chem. Phys. **150**, 154122 (2019).
- <sup>15</sup> P. Verma and D. G. Truhlar, Trends Chem. **2**, 302 (2020), special Issue - Laying Groundwork for the Future.
- <sup>16</sup> M. A. Rohrdanz, K. M. Martins, and J. M. Herbert, J. Chem. Phys. **130**, 054112 (2009).
- <sup>17</sup> S. Mohr, L. E. Ratcliff, L. Genovese, D. Caliste, P. Boulanger, S. Goedecker, and T. Deutsch, Phys. Chem. Chem. Phys. **17**, 31360 (2015).
- <sup>18</sup> M. Bursch, J.-M. Mewes, A. Hansen, and S. Grimme, Angew. Chem. Int. Ed. **61**, e202205735 (2022).
- <sup>19</sup> L. Li, J. C. Snyder, I. M. Pelaschier, J. Huang, U.-N. Nirajan, P. Duncan, M. Rupp, K.-R. Müller, and K. Burke, Int. J. Quantum Chem. **116**, 819 – 833 (2016).
- <sup>20</sup> F. Brockherde, L. Vogt, L. Li, M. E. Tuckerman, K. Burke, and K.-R. Müller, Nat. Commun. **8**, 872 (2017).
- <sup>21</sup> R. Nagai, R. Akashi, and O. Sugino, npj Comput. Mater. **6** (2020).
- <sup>22</sup> S. Dick and M. Fernandez-Serra, Nat. Commun. **11** (2020).
- <sup>23</sup> B. Kalita, L. Li, R. J. McCarty, and K. Burke, Acc. Chem. Res. **54**, 818 (2021).
- <sup>24</sup> J. Kirkpatrick, B. McMorrow, D. H. P. Turban, A. L. Gaunt, J. S. Spencer, A. G. D. G. Matthews, A. Obika, L. Thiry, M. Fortunato, D. Pfau, L. R. Castellanos, S. Petersen, A. W. R. Nelson, P. Kohli, P. Mori-Sánchez, D. Hassabis, and A. J. Cohen, Science **374**, 1385 (2021).
- <sup>25</sup> L. Li, S. Hoyer, R. Pederson, R. Sun, E. D. Cubuk, P. Riley, and K. Burke, Phys. Rev. Lett. **126**, 036401 (2021).
- <sup>26</sup> E. Cuierrier, P.-O. Roy, R. Wang, and M. Ernzerhof, J. Chem. Phys. **157** (2022).
- <sup>27</sup> S. Riemelmoser, C. Verdi, M. Kaltak, and G. Kresse, J. Chem. Theory Comput. **19**, 7287 (2023).
- <sup>28</sup> M. F. Kasim and S. M. Vinko, Phys. Rev. Lett. **127**, 126403 (2021).
- <sup>29</sup> R. Nagai, R. Akashi, and O. Sugino, Phys. Rev. Res. **4**, 013106 (2022).
- <sup>30</sup> J. Wu, S.-M. Pun, X. Zheng, and G. Chen, J. Chem. Phys. **159** (2023).
- <sup>31</sup> X. Zhang and G. K.-L. Chan, J. Chem. Phys. **157**, 204801 (2022).
- <sup>32</sup> P. A. M Casares, J. S. Baker, M. Medvidović, R. d. Reis, and J. M. Arrazola, J. Chem. Phys. **160** (2024).
- <sup>33</sup> B. Kalita, R. Pederson, J. Chen, L. Li, and K. Burke, J. Phys. Chem. Lett. **13**, 2540 (2022).
- <sup>34</sup> J. Schmidt, C. L. Benavides-Riveros, and M. A. Marques, J. Phys. Chem. Lett. **10**, 6425 (2019).
- <sup>35</sup> H. Ma, A. Narayanaswamy, P. Riley, and L. Li, Sci. Adv. **8**, eabq0279 (2022).
- <sup>36</sup> O. Kyriienko, A. E. Paine, and V. E. Elfving, Phys. Rev. A **103**, 052416 (2021).
- <sup>37</sup> A. Abbas, D. Sutter, C. Zoufal, A. Lucchi, A. Figalli, and S. Woerner, Nat. Comput. Sci. **1**, 403 (2021).
- <sup>38</sup> K. Mitarai, M. Negoro, M. Kitagawa, and K. Fujii, Phys. Rev. A **98**, 032309 (2018).
- <sup>39</sup> M. Schuld, V. Bergholm, C. Gogolin, J. Izaac, and N. Killoran, Phys. Rev. A **99**, 032331 (2019).

- <sup>40</sup> O. Kyriienko and V. E. Elfving, Phys. Rev. A **104**, 052417 (2021).
- <sup>41</sup> M. Cerezo, A. Arrasmith, R. Babbush, S. C. Benjamin, S. Endo, K. Fujii, J. R. McClean, K. Mitarai, X. Yuan, L. Cincio, *et al.*, Nat. Rev. Phys. **3**, 625 (2021).
- <sup>42</sup> I. Cong, S. Choi, and M. D. Lukin, Nat. Phys. **15**, 1273 (2019).
- <sup>43</sup> H.-Y. Huang, M. Broughton, J. Cotler, S. Chen, J. Li, M. Mohseni, H. Neven, R. Babbush, R. Kueng, J. Preskill, *et al.*, Science **376**, 1182 (2022).
- <sup>44</sup> M. Schuld, R. Sweke, and J. J. Meyer, Phys. Rev. A **103**, 032430 (2021).
- <sup>45</sup> M. Larocca, P. Czarnik, K. Sharma, G. Muraleedharan, P. J. Coles, and M. Cerezo, Quantum **6**, 824 (2022).
- <sup>46</sup> A. Abbas, R. King, H.-Y. Huang, W. J. Huggins, R. Movassagh, D. Gilboa, and J. R. McClean, arXiv preprint arXiv:2305.13362 (2023).
- <sup>47</sup> K. Beer, D. Bondarenko, T. Farrelly, T. J. Osborne, R. Salzmann, D. Scheiermann, and R. Wolf, Nat. Commun. **11**, 808 (2020).
- <sup>48</sup> S. H. Sack, R. A. Medina, A. A. Michailidis, R. Kueng, and M. Serbyn, PRX Quantum **3**, 020365 (2022).
- <sup>49</sup> H.-Y. Huang, R. Kueng, and J. Preskill, Nat. Phys. **16**, 1050 (2020).
- <sup>50</sup> D. Miller, L. E. Fischer, I. O. Sokolov, P. K. Barkoutsos, and I. Tavernelli, arXiv preprint arXiv:2203.03646 (2022).
- <sup>51</sup> G. Verdon, T. McCourt, E. Luhznica, V. Singh, S. Leichenauer, and J. Hidary, arXiv e-prints , arXiv:1909.12264 (2019).
- <sup>52</sup> M. Schuld, K. Brádler, R. Israel, D. Su, and B. Gupt, Phys. Rev. A **101**, 032314 (2020).
- <sup>53</sup> L.-P. Henry, S. Thabet, C. Dalyac, and L. Henriet, Phys. Rev. A **104**, 032416 (2021).
- <sup>54</sup> S. Thabet, R. Fouilland, and L. Henriet, arXiv preprint arXiv:2210.10610 (2022).
- <sup>55</sup> P. Mernyei, K. Meichanetzidis, and I. I. Ceylan, in *Int. Conf. Mach. Learn.* (PMLR, 2022) pp. 15401–15420.
- <sup>56</sup> B. Albrecht, C. Dalyac, L. Leclerc, L. Ortiz-Gutiérrez, S. Thabet, M. D’Arcangelo, J. R. Cline, V. E. Elfving, L. Lassablière, H. Silvério, *et al.*, Phys. Rev. A **107**, 042615 (2023).
- <sup>57</sup> A. Skolik, M. Cattelan, S. Yarkoni, T. Bäck, and V. Dunjko, npj Quantum Inf. **9**, 47 (2023).
- <sup>58</sup> Q. T. Nguyen, L. Schatzki, P. Braccia, M. Ragone, P. J. Coles, F. Sauvage, M. Larocca, and M. Cerezo, arXiv preprint arXiv:2210.08566 (2022).
- <sup>59</sup> L. Schatzki, M. Larocca, F. Sauvage, and M. Cerezo, arXiv preprint arXiv:2210.09974 (2022).
- <sup>60</sup> J. J. Meyer, M. Mularski, E. Gil-Fuster, A. A. Mele, F. Arzani, A. Wilms, and J. Eisert, PRX Quantum **4**, 010328 (2023).
- <sup>61</sup> M. T. West, M. Sevior, and M. Usman, Mach. Learn. Sci. Technol. **4**, 035027 (2023).
- <sup>62</sup> I. N. M. Le, O. Kiss, J. Schuhmacher, I. Tavernelli, and F. Tacchino, arXiv preprint arXiv:2311.11362 (2023).
- <sup>63</sup> A. Pesah, M. Cerezo, S. Wang, T. Volkoff, A. T. Sornborger, and P. J. Coles, Phys. Rev. X **11**, 041011 (2021).
- <sup>64</sup> E. R. Anschuetz, A. Bauer, B. T. Kiani, and S. Lloyd, Quantum **7**, 1189 (2023).
- <sup>65</sup> B. Senjean, S. Yalouz, and M. Saubanère, SciPost Physics **14**, 055 (2023).
- <sup>66</sup> M. Rossmannek, P. K. Barkoutsos, P. J. Ollitrault, and I. Tavernelli, J. Chem. Phys. **154** (2021).
- <sup>67</sup> R. Schade, C. Bauer, K. Tamoev, L. Mazur, C. Plessl, and T. D. Kühne, Physical Review Research **4**, 033160 (2022).
- <sup>68</sup> “A patent application for the method described in this manuscript has been submitted by PASQAL SAS.” (2024).
- <sup>69</sup> P. Hohenberg and W. Kohn, Phys. Rev. **136**, B864 (1964).
- <sup>70</sup> J. Schmidt, C. L. Benavides-Riveros, and M. A. Marques, J. Phys. Chem. Lett. **10**, 6425 (2019).
- <sup>71</sup> K. Hornik, M. Stinchcombe, and H. White, Neural Netw. **2**, 359 (1989).
- <sup>72</sup> M. Cerezo, A. Sone, T. Volkoff, L. Cincio, and P. J. Coles, Nat. Comm. **12**, 1791 (2021).
- <sup>73</sup> A. Pérez-Salinas, A. Cervera-Lierta, E. Gil-Fuster, and J. I. Latorre, Quantum **4**, 226 (2020).
- <sup>74</sup> A. Pérez-Salinas, D. López-Núñez, A. García-Sáez, P. Forn-Díaz, and J. I. Latorre, Phys. Rev. A **104**, 012405 (2021).
- <sup>75</sup> S. Dasgupta and J. M. Herbert, J. Comput. Chem. **38**, 869 (2017).
- <sup>76</sup> J. Landman, S. Thabet, C. Dalyac, H. Mhiri, and E. Kashefi, arXiv preprint arXiv:2210.13200 (2022).
- <sup>77</sup> J. Bradbury, R. Frostig, P. Hawkins, M. J. Johnson, C. Leary, D. Maclaurin, G. Necula, A. Paszke, J. Vander-Plas, S. Wanderman-Milne, and Q. Zhang, “JAX: composable transformations of Python+NumPy programs,” (2018).
- <sup>78</sup> A. Paszke, S. Gross, S. Chintala, G. Chanan, E. Yang, Z. DeVito, Z. Lin, A. Desmaison, L. Antiga, and A. Lerer, (2017).
- <sup>79</sup> Q. Sun, T. C. Berkelbach, N. S. Blunt, G. H. Booth, S. Guo, Z. Li, J. Liu, J. D. McClain, E. R. Sayfutyarova, S. Sharma, *et al.*, Wiley Interdiscip. Rev. Comput. Mol. Sci. **8**, e1340 (2018).
- <sup>80</sup> T. Helgaker, P. Jorgensen, and J. Olsen, *Molecular electronic-structure theory* (John Wiley & Sons, 2013).
- <sup>81</sup> J.-D. Chai, J. Chem. Phys. **136**, 154104 (2012).
- <sup>82</sup> E. Cancès, K. N. Kudin, G. E. Scuseria, and G. Turinici, J. Chem. Phys. **118**, 5364 (2003).
- <sup>83</sup> R. J. Bartlett and M. Musial, Rev. Mod. Phys. **79**, 291 (2007).
- <sup>84</sup> D. P. Kingma and J. Ba, arXiv preprint arXiv:1412.6980 (2014).
- <sup>85</sup> C. Zhu, R. H. Byrd, P. Lu, and J. Nocedal, ACM Transactions on mathematical software (TOMS) **23**, 550 (1997).
- <sup>86</sup> D. Seitz, N. Heim, J. P. Moutinho, R. Guichard, V. Abramavicius, A. Wennersteen, G.-J. Both, A. Quelle, C. de Groot, G. V. Velikova, V. E. Elfving, and M. Dagrada, arXiv:2401.09915 (2024).
- <sup>87</sup> D. K. Park, F. Petruccione, and J.-K. K. Rhee, Sci. Rep. **9**, 3949 (2019).
- <sup>88</sup> I. W. Bulik, T. M. Henderson, and G. E. Scuseria, J. Chem. Theory Comput. **11**, 3171 (2015).
- <sup>89</sup> I. O. Sokolov, P. K. Barkoutsos, P. J. Ollitrault, D. Greenberg, J. Rice, M. Pistoia, and I. Tavernelli, J. Chem. Phys. **152** (2020).
- <sup>90</sup> A. Peruzzo, J. McClean, P. Shadbolt, M.-H. Yung, X.-Q. Zhou, P. J. Love, A. Aspuru-Guzik, and J. L. O’Brien, Nat. Commun. **5**, 4213 (2014).
- <sup>91</sup> S. McArdle, T. Jones, S. Endo, Y. Li, S. C. Benjamin, and X. Yuan, npj Quantum Inf. **5**, 75 (2019).
- <sup>92</sup> S. Thabet, R. Fouilland, M. Djellabi, I. Sokolov, S. Kasturne, L.-P. Henry, and L. Henriet, arXiv preprint arXiv:2310.20519 (2023).

- <sup>93</sup> B. Jaderberg, A. A. Gentile, Y. A. Berrada, E. Shishenina, and V. E. Elfving, arXiv preprint arXiv:2309.03279 (2023).
- <sup>94</sup> A. E. Paine, V. E. Elfving, and O. Kyriienko, Phys. Rev. A **107**, 032428 (2023).
- <sup>95</sup> L. Henriet, L. Beguin, A. Signoles, T. Lahaye, A. Browaeys, G.-O. Reymond, and C. Jurczak, Quantum **4**, 327 (2020).
- <sup>96</sup> L.-P. Henry, S. Thabet, C. Dalyac, and L. Henriet, Physical Review A **104**, 032416 (2021).
- <sup>97</sup> A. E. Paine, V. E. Elfving, and O. Kyriienko, arXiv preprint arXiv:2308.01827 (2023).
- <sup>98</sup> V. Lebedev, USSR Computational Mathematics and Mathematical Physics **15**, 44 (1975).
- <sup>99</sup> M. Schuld and F. Petruccione, *Supervised learning with quantum computers*, Vol. 17 (Springer, 2018).